Int J Fract (2010) 161:97–119
DOI 10.1007/s10704-009-9432-6

ORIGINAL PAPER

A comparative study on the modelling of discontinuous fracture by means of enriched nodal and element techniques and interface elements

D. Dias-da-Costa · J. Alfaiate · L. J. Sluys · E. Júlio

Received: 31 July 2009 / Accepted: 5 November 2009 / Published online: 26 November 2009
© Springer Science+Business Media B.V. 2009

Abstract In this paper, three different approaches used to model strong discontinuities are studied: a new strong embedded discontinuity technique, designated as the discrete strong embedded discontinuity approach (*DSDA*), introduced in Dias-da-Costa et al. (Eng Fract Mech 76(9):1176–1201, 2009); the generalized finite element method, (*GFEM*), developed by Duarte and Oden (Tech Rep 95-05, 1995) and Belytschko and Black (Int J Numer Methods Eng 45(5):601–620, 1999); and the use of interface elements (Hillerborg et al. in Cem Concr Res 6(6): 773–781, 1976). First, it is shown that all three descriptions are based on the same variational formulation. However, the main differences between these models lie in the way the discontinuity is represented in the finite element mesh, which is explained in the paper. Main focus is on the differences between the element enrichment technique, used in the *DSDA* and the nodal enrichment technique adopted in the *GFEM*. In both cases, global enhanced degrees of freedom are adopted. Next, the numerical integration of the discretised equations in the three methods is addressed and some important differences are discussed. Two types of numerical tests are presented: first, simple academic examples are used to emphasize the differences found in the formulations and next, some benchmark tests are computed.

Keywords Strong embedded discontinuity · Discrete crack approach · Generalized finite element method

D. Dias-da-Costa (✉) · E. Júlio
ISISE, Civil Engineering Department,
University of Coimbra, Rua Luís Reis Santos,
3030-788 Coimbra, Portugal
e-mail: dcosta@dec.uc.pt

J. Alfaiate
ICIST, Civil Engineering Department,
Instituto Superior Técnico, Av. Rovisco Pais, 1049-001
Lisboa, Portugal

L. J. Sluys
Civil Engineering Department, Engineering and Geosciences,
Delft University of Technology, P.O. Box 5048,
2600 GA Delft, The Netherlands

List of Symbols

$\mathbf{a}$	Total displacement vector at the nodes
$\hat{\mathbf{a}}$	Regular displacement vector at the nodes
$\hat{\mathbf{a}}_2$	Regular displacement vector for the enriched layer at the nodes
$\tilde{\mathbf{a}}$	Enhanced displacement vector at the nodes
$\tilde{\mathbf{a}}_{rb}$	Rigid body motion part of the enhanced displacement vector at the nodes
$\bar{\mathbf{b}}$	Body forces vector
$\mathbf{B}$	Strain-nodal displacement matrix
$\mathbf{B}_w$	Enhanced strain-nodal displacement matrix
c	Absolute value of the jump
c_0	Cohesion
d	Scalar damage
$\mathbf{D}$	Constitutive matrix

D_{s0}	Initial elastic shear stiffness
$D_{s\kappa}$	Shear stiffness for an advanced state of damage
E	Young's modulus
f	Loading function
$\hat{\mathbf{f}}$	Regular external vector force at the regular nodes
$\tilde{\mathbf{f}}$	Enhanced external vector force at the regular nodes
f_t	Tensile strength
$\mathbf{f}_w$	External vector force at the additional nodes
G_F	Fracture energy
h_s	Parameter defined by: $-\ln(D_{s\kappa}/D_{s0})$
$\mathcal{H}_{\Gamma_d}$	Heaviside function
$\mathbf{H}_{\Gamma_d}$	Diagonal matrix containing the Heaviside function evaluated at each degree of freedom
$\mathbf{I}$	Identity matrix
k_n, k_s	Normal and shear penalty parameters, respectively
κ	Scalar variable depending on the normal and shear jump components
k_0	Parameter denoting the beginning of the softening
$\mathbf{K}_{aa}, \mathbf{K}_{\hat{a}\hat{a}}$	Bulk stiffness matrices for the DSDA and GFEM
$\mathbf{K}_{aw}, \mathbf{K}_{wa}, \mathbf{K}_{ww}$	Enhanced bulk stiffness matrices for the DSDA
$\mathbf{K}_{\hat{a}\tilde{a}}, \mathbf{K}_{\tilde{a}\hat{a}}, \mathbf{K}_{\tilde{a}\tilde{a}}$	Enhanced bulk stiffness matrices for the GFEM
$\mathbf{K}_d$	Discontinuity stiffness matrix
l	Measure of distance around the tip
l_{ch}	Hillerborg's characteristic length
l_d	Discontinuity length
$\mathbf{L}$	Differential operator matrix
$\mathbf{L_w}$	Matrix used to compute the difference between top and bottom displacements for a discrete-interface
$\mathbf{m}$	Jump direction vector
$\mathbf{M}_w$	Rigid body motion matrix
$\mathbf{M}_w^k$	Matrix composed by evaluating the rigid body motion matrix at each finite element node
n	Number of the finite element nodes
$\mathbf{n}$	Unit vector normal to the boundary
$\mathbf{n}^+$	Unit vector normal to the discontinuity surface
n_w	Number of additional nodes located at the discontinuity for jump interpolation
$\mathbf{N}_w$	Shape function matrix for the jumps
P	External load
P_h	Horizontal external load
r	Distance between the integration point and the discontinuity tip
$\mathbf{s}, \mathbf{n}$	Unit vectors tangent and orthogonal to the discontinuity, respectively
$\mathbf{t}$	Traction vector
$\bar{\mathbf{t}}$	Natural forces vector
$\mathbf{T}$	Discontinuity constitutive matrix
$\mathbf{T}_{el}$	Elastic discontinuity constitutive matrix
$\mathbf{u}$	Total displacement vector
$\bar{\mathbf{u}}$	Essential boundary conditions vector
$\hat{\mathbf{u}}$	Regular displacement field vector
$\hat{\mathbf{u}}_2$	Regular displacement field vector for the enriched layer
$\tilde{\mathbf{u}}$	Enhanced displacement field vector
$[\![\mathbf{u}]\!]$	Jump vector
u_v	Vertical displacement
$\mathbf{w}$	Nodal jump vector
w_i	Weight for the integration point i
$\mathbf{x}$	Global coordinates of a material point
$\mathbf{x}_1, \mathbf{x}_2$	Global frame
α	Discontinuity angle
β	Shear contribution parameter
Γ	Boundary
Γ_d	Discontinuity surface
Γ_t	Boundary with natural forces
Γ_u	Boundary with essential conditions
$\boldsymbol{\varepsilon}$	Total strain tensor
$\hat{\boldsymbol{\varepsilon}}$	Regular strain tensor
ρ	Dead –weight
$\boldsymbol{\sigma}$	Stress tensors
σ_I	First principle stress
ν	Poisson ratio
Ω	Elastic domain
$d(\cdot)$	Incremental variation of $(\cdot)$
$(\cdot)^s$	Symmetric part of $(\cdot)$
$\delta(\cdot)$	Admissible or virtual variation of $(\cdot)$
δ_{Γ_d}	Dirac's delta–function along the surface Γ_d
$(\cdot)^e$	$(\cdot)$ belonging to the finite element e
$(\cdot)^+, (\cdot)^-$	$(\cdot)$ at the positive and negative side of the discontinuity, respectively
$(\cdot)_n, (\cdot)_s$	Normal and shear component of $(\cdot)$
$\otimes$	Dyadic product
$\langle\cdot\rangle^+$	McAuley brackets

1 Introduction

Numerical modelling of fracture behaviour of quasi–brittle materials remains an important topic nowadays. In these materials, the progressive development of microcracking, due to increase of damage, leads to a decrease of the load bearing capacity. The fracture zone ahead of the crack tip can extend for a length several times longer than the maximum aggregate size, rendering the assumptions of linear elastic fracture mechanics inadequate.

Nonlinear fracture mechanics in quasi–brittle materials was introduced by Hillerborg et al. (1976), following the works from Dugdale (1960) and Barenblatt (1962). His fictitious crack model was presented within the scope of the discrete crack approach. Afterwards, the smeared crack approach was introduced by Bazant and Oh (1983), in which continuum models were adopted to describe the fracture behaviour. Both approaches were considerably developed since then, the latter giving rise to regularised models, such as non–local or gradient models, whereas the former evolved into strong discontinuity formulations.

The development of finite elements with strong embedded discontinuities became a powerful technique for the efficient modelling of strain localization (Simo and Rifai 1990; Dvorkin et al. 1990; Klisinski et al. 1991; Simo et al. 1993; Lofti and Shing 1995; Larsson and Runesson 1996; Oliver 1996; Armero and Garikipati 1996; Wells and Sluys 2000; Oliver et al. 2002; Sancho et al. 2005). The element enrichment is performed in the displacement field allowing to incorporate localized strain modes. These formulations are local and therefore a static condensation can be performed at element level, thus keeping the number of degrees of freedom constant. Moreover, use of constant strain triangles with constant jumps across the discontinuity is made. As a consequence, the patch test is satisfied and Simo's orthogonality condition (Simo and Rifai 1990) is automatically fulfilled. In Bolzon (2001) and Linder and Armero (2007), linear jump fields are introduced in the embedded discontinuities; these formulations do not satisfy the orthogonality condition and still remain local, with non–continuum jumps across the element boundaries.

The embedded discontinuity approach adopted herein, designated the Discrete Strong Discontinuity Approach, *DSDA* (Alfaiate et al. 2003; Alfaiate and Sluys 2005; Dias-da-Costa et al. 2009), is significantly different from the previous ones. This is due to the following specific features: i) the *DSDA* is based on a discrete approach, ii) a one dimensional interface element is explicitly embedded in the parent element to model the discontinuity, iii) a non-homogeneous jump displacement field is introduced in each parent element, which is approximated by the shape functions of the interface element, iv) the additional degrees of freedom are located at the discontinuity, v) these additional degrees of freedom are global, vi) both continuous jumps and tractions across element boundaries are obtained and vii) the enhanced displacement field induced by the jumps consists of a rigid body motion. For clarity, in the following, the former strong discontinuity approach (Simo and Rifai 1990; Dvorkin et al. 1990; Klisinski et al. 1991) will be designated as the *EAS* approach, whereas the present approach will be referred to as *DSDA*.

Almost simultaneously, the works presented by Duarte and Oden (1995) and Melenk and Babuška (1996), and next by Belytschko and Black (1999) and Moës et al. (1999), gave rise to the generalized finite element method (*GFEM*) (Duarte et al. 2000), also known as the extended finite element method (XFEM). With this method, it is possible to include *a priori* some knowledge on the local behaviour of the solution in the finite element space to represent discontinuities. Belytschko and Black (1999) and Moës et al. (1999; 2000) applied the *GFEM* to linear elastic fracture mechanics problems, whereas Wells and Sluys (2001a) extended the method to cohesive cracks and Areias and Belytschko (2005) to three-dimensional crack propagation. The *GFEM* is based on a nodal enrichment technique, whereas an element enrichment technique is adopted in the embedded approaches. Consequently, more degrees of freedom are needed to model the discontinuity with the *GFEM* than with the *DSDA*.

Jirásek and Belytschko (2002), Oliver et al. (2006) and Borja (2008) performed a comparative analysis between: i) a local embedded formulation, using static condensation, based on the enhanced assumed strain method (*EAS*) and ii) the *GFEM*. In Jirásek and Belytschko (2002) both cracks and shear bands are dealt with, whereas in Borja (2008) only frictional crack propagation is considered and mode-I fracture is not covered. In Oliver et al. (2006), a considerable number of tests is presented and some issues related to the performance of the numerical analysis are discussed.

In this paper, three strong discontinuity descriptions are compared: the discrete-interface approach, the *DSDA* and the *GFEM*. Note that, as mentioned above, the *DSDA* cannot be considered a subclass or a variant of the *EAS* approach. In fact the *DSDA* shares many attributes from the discrete approach with interfaces, and this is why a comparison between both is presented herein. Further discussion related to the main differences between the *EAS* approach and the *DSDA* can be found in Dias-da-Costa et al. (2009). All formulations aim at modelling the same problem consisting of a continuum crossed by a discontinuity, which can be interpreted as an internal boundary dividing a domain into two parts. With the discrete-interface approach, interface elements located at interelement boundaries are used to model the discontinuity. With this formulation it is possible to obtain: *i*) mesh objectivity with prescribed cracks; and *ii*) true representation of strong discontinuities. This is why it is also considered here as a reference solution in some particular cases. However, it is well known that with non–prescribed cracks, either remeshing must be performed (Ingraffea 1989), or a projection of the *true* crack has to be made on the fixed interelement boundaries, giving rise to approximated crack paths (Alfaiate et al. 1997).

In Sect. 2, it is shown that the variational formulation introduced by Malvern (1969), for a continuum crossed by a discontinuity, applies to all three descriptions. The main differences among these methods are related to the discontinuity representation in the finite element mesh. In Sects. 2.3.1–2.3.3, the finite element approximation and the discretised equations are presented. In these Sections, special attention is given to the implementation of both the *DSDA* element enrichment technique and the *GFEM* nodal enrichment technique. In particular, the possibility of imposing boundary conditions at the discontinuity in case of the *DSDA* is addressed.

The three descriptions are also investigated with respect to the numerical integration of the discretised equations. This issue is addressed in Sects. 4.2 and 5.2.5, in which oscillatory solutions can be found when some particular integration schemes are adopted. These problems are well known for some time for interface elements, for which solutions exist (Kikuchi and Oden 1988), which are applied here to the *DSDA* and the *GFEM*. In Sect. 5.1, some academic examples are computed and in Sect. 5.2 results obtained from some benchmark tests with all the formulations are also compared. Finally, advantages and disadvantages of using the discrete-interface approach, the *DSDA* or the *GFEM*, in the scope of the strong discontinuity framework are discussed.

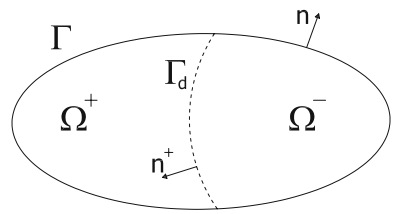

Fig. 1 Domain Ω crossed by a discontinuity surface Γ_d

2 Problem description

The discrete-interface approach has been widely used in the past and this is why a brief description is presented herein. Regarding this topic, the reader may be referred to the works presented in Malvern (1969), Goodman et al. (1968), Hillerborg et al. (1976), Hermann (1978), Ingraffea and Saouma (1985), Bocca et al. (1986), Kikuchi and Oden (1988), Alfaiate et al. (1992), Carol and Prat (1995), Lourenço and Rots (1997), Carey and Ma (1999), Tijssens et al. (2000), Dias-da-Costa et al. (2009). In the following, emphasis is put on the descriptions of both the *DSDA* and the *GFEM*.

2.1 Kinematics of a strong discontinuity

In this section the kinematics of a strong discontinuity is addressed. An elastic domain Ω, with boundary Γ, is crossed by a discontinuity surface Γ_d dividing it into two subregions, Ω^+ and Ω^-, according to Fig. 1.

A quasi–static loading is applied to the body, consisting of body forces, $\bar{\mathbf{b}}$, and natural boundary conditions, $\bar{\mathbf{t}}$, the latter distributed on the external boundary, Γ_t. The essential boundary conditions $\bar{\mathbf{u}}$ are then applied in the remaining part of the boundary, Γ_u, such that $\Gamma_t \cup \Gamma_u = \Gamma$ and $\Gamma_t \cap \Gamma_u = \varnothing$. The vector $\mathbf{n}$ is orthogonal to the boundary surface, pointing outwards, while $\mathbf{n}^+$ is orthogonal to the internal discontinuity surface, pointing inwards Ω^+.

For each material point in Ω, the total displacement $\mathbf{u}$ is evaluated as the sum of two parts: the regular displacement field $\hat{\mathbf{u}}$; and the enhanced displacement field $\tilde{\mathbf{u}}$, induced by the jumps in the discontinuity Γ_d:

$$\mathbf{u}(\mathbf{x}) = \hat{\mathbf{u}}(\mathbf{x}) + \mathcal{H}_{\Gamma_d}\tilde{\mathbf{u}}(\mathbf{x}), \tag{1}$$

where $\mathcal{H}_{\Gamma_d}$ is a function defining the way the jump is transmitted by the discontinuity. This transmission to Ω^+ and Ω^- can be done according to a scalar factor (Klisinski et al. 1991; Lofti and Shing 1995; Ohlsson and Olofsson 1997; Alfaiate et al. 2003; Remmers 2006) or alternatively by using independent enhanced displacement fields, $\tilde{\mathbf{u}}^+$ and $\tilde{\mathbf{u}}^-$ (Bolzon 2001; Alfaiate and Sluys 2004). The Heaviside function used to transmit the total jump is defined as:

$$\mathcal{H}_{\Gamma_d} = \begin{cases} 1 & \text{if } \mathbf{x} \in \Omega^+ \\ 0 & \text{otherwise.} \end{cases} \tag{2}$$

Adopting small displacements, the strain field is given by:

$$\begin{aligned} \boldsymbol{\varepsilon} &= \boldsymbol{\nabla}^s\mathbf{u} \\ &= \underbrace{\boldsymbol{\nabla}^s\hat{\mathbf{u}} + \mathcal{H}_{\Gamma_d}\left(\boldsymbol{\nabla}^s\tilde{\mathbf{u}}\right)}_{\text{bounded}} + \underbrace{\delta_{\Gamma_d}\left([\![\mathbf{u}]\!] \otimes \mathbf{n}\right)^s}_{\text{unbounded}} \quad \text{in } \Omega, \end{aligned} \tag{3}$$

where $(\cdot)^s$ refers to the symmetric part of $(\cdot)$ and $\otimes$ denotes the dyadic product. Both the displacement and the strain fields are continuous in Ω^- and Ω^+, since the unbounded term in Eq. (3) vanishes in $\Omega\backslash\Gamma_d = \Omega^- \cup \Omega^+$.

The jump is obtained by evaluating the enhanced displacement field along the discontinuity according to:

$$[\![\mathbf{u}]\!] = \tilde{\mathbf{u}}_{|\Gamma_d}, \tag{4}$$

and it is usual to represent the jump $[\![\mathbf{u}]\!]$ in the following form:

$$[\![\mathbf{u}]\!] = c\mathbf{m}, \tag{5}$$

with c and $\mathbf{m}$ representing, respectively, the modulus and direction of the jump. When $\mathbf{m}$ is parallel to $\mathbf{n}^+$, the crack opens in pure mode-I; if $\mathbf{m}$ is parallel to the crack, mode-II failure is obtained.

2.2 Variational formulation

The variational formulation presented by Malvern (1969) is adopted here, since it is valid for all three discrete descriptions:

$$\begin{aligned} &\int_{\Omega\backslash\Gamma_d} (\boldsymbol{\nabla}^s\delta\mathbf{u}) : \boldsymbol{\sigma}(\boldsymbol{\varepsilon})d\Omega + \int_{\Gamma_d} \delta[\![\mathbf{u}]\!] \cdot \mathbf{t}^+ d\Gamma \\ &= \int_{\Omega\backslash\Gamma_d} \delta\mathbf{u} \cdot \bar{\mathbf{b}} d\Omega + \int_{\Gamma_t} \delta\mathbf{u} \cdot \bar{\mathbf{t}} d\Gamma, \end{aligned} \tag{6}$$

where $\delta\mathbf{u}$ is the admissible displacement variation, and $\delta[\![\mathbf{u}]\!]$ is the admissible jump variation and $\mathbf{t}^+$ is the traction applied at the discontinuity.

This weak formulation is usually adopted for the discrete-interface approach, but it is also the basis for both *DSDA* and the *GFEM* descriptions. The virtual displacements $\delta\mathbf{u}$ are decomposed into the regular and enhanced parts, according to Eq. (1):

$$\delta\mathbf{u} = \delta\hat{\mathbf{u}} + \mathcal{H}_{\Gamma_d}\delta\tilde{\mathbf{u}}. \tag{7}$$

Substituting this Eq. (7) in Eq. (6) and by taking successively: *i)* $\delta\hat{\mathbf{u}} = \mathbf{0}$ and *ii)* $\delta\tilde{\mathbf{u}} = \mathbf{0}$, with $\delta\tilde{\mathbf{u}}_{|\Gamma_d} = \delta[\![\mathbf{u}]\!]$, the following Eqs. are obtained:

$$\int_{\Omega\backslash\Gamma_d} (\boldsymbol{\nabla}^s\delta\hat{\mathbf{u}}) : \boldsymbol{\sigma}(\boldsymbol{\varepsilon})d\Omega = \int_{\Omega\backslash\Gamma_d} \delta\hat{\mathbf{u}} \cdot \bar{\mathbf{b}} d\Omega + \int_{\Gamma_t} \delta\hat{\mathbf{u}} \cdot \bar{\mathbf{t}} d\Gamma, \tag{8a}$$

$$\int_{\Omega^+} (\boldsymbol{\nabla}^s\delta\tilde{\mathbf{u}}) : \boldsymbol{\sigma}(\boldsymbol{\varepsilon})d\Omega + \int_{\Gamma_d} \delta[\![\mathbf{u}]\!] \cdot \mathbf{t}^+ d\Gamma = \int_{\Omega^+} \delta\tilde{\mathbf{u}} \cdot \bar{\mathbf{b}} d\Omega + \int_{\Gamma_{t^+}} \delta\tilde{\mathbf{u}} \cdot \bar{\mathbf{t}} d\Gamma. \tag{8b}$$

Eqs. (8a) and (8b) lead to a consistent weak formulation as well as to symmetry, if the adopted constitutive laws are also symmetric. This is usually the case when traction continuity is enforced in a weak sense by Eq. (8b).

2.3 Numerical implementation

Although both the *DSDA* and the *GFEM* share a common variational framework, represented in Eqs. (8a) and (8b), the *DSDA* remains an element enrichment technique, whereas in the *GFEM* nodal enrichment is adopted. Therefore, different discretised equations are obtained, which are derived separately in the following.

2.3.1 Discretisation in the DSDA

In the *DSDA*, the enhanced displacement field is a rigid body motion. As a consequence, the gradient of both the enhanced trial displacement field and the infinitesimal admissible displacement field are null: $\boldsymbol{\nabla}^s\tilde{\mathbf{u}} = \boldsymbol{\nabla}^s\delta\tilde{\mathbf{u}} = \mathbf{0}$. Equations (8a) and (8b) take into account the contribution of the bulk and of the discontinuity, respectively. Similar to the discrete-interface approach, these equations become independent. As a consequence, Simo's

orthogonality condition (Simo and Rifai 1990) is fulfilled exactly and the enhanced stress field is eliminated from the equations.

In order to clearly establish the similitude between the *DSDA* and the discrete-interface approach, the discretised equations were derived independently for the bulk and for the discontinuity in Dias-da-Costa et al. (2009). However, in this article, the final coupled system of equations is derived directly from the variational statement, enabling a straight comparison with both the *GFEM* and previous embedded discontinuity formulations.

The displacement field in each element is given by:

$$\mathbf{u}^e = \mathbf{N}^e(\mathbf{x})\left(\hat{\mathbf{a}}^e + \mathcal{H}_{\Gamma_d}\tilde{\mathbf{a}}^e\right) \quad \text{if } \mathbf{x} \in \Omega^e \backslash \Gamma_d, \tag{9a}$$

$$[\![\mathbf{u}]\!]^e = \mathbf{N}^e_w\,[s(\mathbf{x})]\,\mathbf{w}^e \quad \text{at } \Gamma^e_d, \tag{9b}$$

where $\mathbf{N}^e$ contains the usual element shape functions, $\hat{\mathbf{a}}^e$ are the nodal degrees of freedom associated with $\hat{\mathbf{u}}^e$, $\mathbf{N}^e_w$ are the shape functions used to approximate the jumps $[\![\mathbf{u}]\!]^e$ which, in turn, are approximated by the degrees of freedom $\mathbf{w}^e$, measured at the n_w additional nodes. $\mathbf{N}^e_w$ is a $(2 \times n_w)$ matrix. For linear jump interpolation, $n_w = 2$, and $\mathbf{N}^e_w$ contains linear shape functions.

The displacement jumps, measured at the discontinuity, must be transfered to the element nodes, giving rise to the enhanced nodal displacements $\tilde{\mathbf{a}}^e$. For this purpose, the following kinematical relation is adopted:

$$\tilde{\mathbf{a}}^e = \mathbf{M}^{ek}_w \mathbf{w}^e. \tag{10}$$

In Eq. (10), matrix $\mathbf{M}^{ek}_w$ is formed by stacking in rows the rigid body motion matrix $\mathbf{M}^e_w$, evaluated at each of the n nodes of the element ($k = 1, n$), and defined according to:

$$\mathbf{M}^{eT}_w = \begin{bmatrix} 1 - \frac{((x_2 - x_2^i)\sin\alpha)}{l_d} & \frac{(x_1 - x_1^i)\sin\alpha}{l_d} \\ \frac{(x_2 - x_2^i)\cos\alpha}{l_d} & 1 - \frac{(x_1 - x_1^i)\cos\alpha}{l_d} \\ \frac{(x_2 - x_2^i)\sin\alpha}{l_d} & -\frac{(x_1 - x_1^i)\sin\alpha}{l_d} \\ -\frac{(x_2 - x_2^i)\cos\alpha}{l_d} & \frac{(x_1 - x_1^i)\cos\alpha}{l_d} \end{bmatrix}, \tag{11}$$

where α is represented in Fig. 2, and l_d is the length of the discontinuity Γ^e_d measured along the local frame $\mathbf{s}$.

Let the unknowns be $\mathbf{a}^e$ and $\mathbf{w}^e$, where $\mathbf{a}^e$ are the total displacements obtained at the regular nodes k. The incremental stress field is:

$$d\boldsymbol{\sigma}^e = \mathbf{D}^e\mathbf{B}^e(d\mathbf{a}^e - \mathbf{H}^e_{\Gamma_d}\mathbf{M}^{ek}_w d\mathbf{w}^e), \tag{12}$$

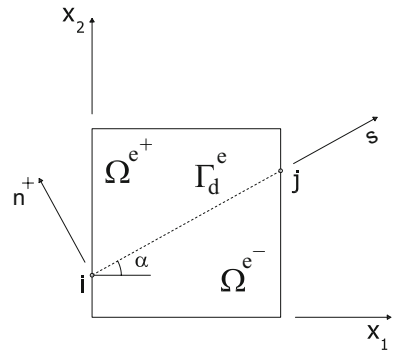

Fig. 2 Domain Ω^e crossed by a discontinuity surface Γ^e_d

in which $\mathbf{D}^e$ is the constitutive matrix, $\mathbf{B}^e$ is the strain-nodal displacement matrix and $\mathbf{H}^e_{\Gamma_d}$ is a $(2n \times 2n)$ diagonal matrix composed by successively evaluating the Heaviside function at each of the $2n$ degrees of freedom of the finite element.

At the discontinuity, and similarly to the discrete-interface approach, the tractions are obtained from the traction-jump law. In incremental format this reads:

$$d\mathbf{t}^e = \mathbf{T}^e d[\![\mathbf{u}]\!]^e = \mathbf{T}^e\mathbf{N}^e_w d\mathbf{w}^e \quad \text{at } \Gamma^e_d, \tag{13}$$

where $\mathbf{T}^e$ is the discontinuity constitutive matrix.

The approximation of the trial displacement field, expressed by Eq. (9a), can be written using the unknowns $\mathbf{a}^e$ and $\mathbf{w}^e$:

$$\mathbf{u}^e = \mathbf{N}^e(\mathbf{x})\left(\mathbf{a}^e + \left(\mathcal{H}_{\Gamma_d}\mathbf{M}^{ek}_w - \mathbf{H}^e_{\Gamma_d}\mathbf{M}^{ek}_w\right)\mathbf{w}^e\right) \quad \text{if } \mathbf{x} \in \Omega^e \backslash \Gamma_d. \tag{14}$$

By using Eqs. (10) and (12)–(14), Eq. (6) is discretised taking successively, *i)* $\delta d\mathbf{w}^e = \mathbf{0}$ and *ii)* $\delta d\mathbf{a}^e = \mathbf{0}$, into the following system of Eqs.:

$$\mathbf{K}^e_{aa} d\mathbf{a}^e - \mathbf{K}^e_{aw} d\mathbf{w}^e = d\hat{\mathbf{f}}^e, \tag{15a}$$

$$-\mathbf{K}^e_{wa} d\mathbf{a}^e + \left(\mathbf{K}^e_{ww} + \mathbf{K}^e_d\right) d\mathbf{w}^e = d\mathbf{f}^e_w - (\mathbf{H}^e_{\Gamma_d}\mathbf{M}^{ek}_w)^T d\hat{\mathbf{f}}^e, \tag{15b}$$

where:

$$\mathbf{K}^e_{aa} = \int_{\Omega^e \backslash \Gamma^e_d} \mathbf{B}^{eT}\mathbf{D}^e\mathbf{B}^e d\Omega, \tag{16}$$

$$\mathbf{K}^e_{aw} = \int_{\Omega^e \backslash \Gamma^e_d} \mathbf{B}^{eT}\mathbf{D}^e\mathbf{B}^e_w d\Omega^e, \tag{17}$$

$$\mathbf{K}^e_{wa} = \mathbf{K}^{eT}_{aw}, \tag{18}$$

$$\mathbf{K}^e_{ww} = \int_{\Omega^e \backslash \Gamma^e_d} \mathbf{B}^{eT}_w\mathbf{D}^e\mathbf{B}^e_w d\Omega^e, \tag{19}$$

$$\mathbf{K}_d^e = \int_{\Gamma_d^e} \mathbf{N}_w^{e\,T} \mathbf{T}^e \mathbf{N}_w^e d\Gamma, \tag{20}$$

with:

$$\mathbf{B}_w^e = \mathbf{B}^e \mathbf{H}_{\Gamma_d}^e \mathbf{M}_w^{ek}, \tag{21}$$

and the external forces are:

$$d\hat{\mathbf{f}}^e = \int_{\Omega^e \backslash \Gamma_d^e} \mathbf{N}^{eT} d\bar{\mathbf{b}}^e d\Omega + \int_{\Gamma_t^e} \mathbf{N}^{eT} d\bar{\mathbf{t}}^e d\Gamma, \tag{22a}$$

$$d\mathbf{f}_w^e = \int_{\Omega^{e+}} \left(\mathbf{M}_w^{ek}\right)^T \mathbf{N}^{eT} d\bar{\mathbf{b}}^e d\Omega + \int_{\Gamma_t^{e+}} \left(\mathbf{M}_w^{ek}\right)^T \mathbf{N}^{eT} d\bar{\mathbf{t}}^e d\Gamma. \tag{22b}$$

If the body forces are neglected and the external forces are applied at the nodes, then $d\mathbf{f}_w^e - (\mathbf{H}_{\Gamma_d}^e \mathbf{M}_w^{ek})^T d\hat{\mathbf{f}}^e = \mathbf{0}$, and only the *regular* nodal forces $d\hat{\mathbf{f}}^e$ need to be computed. In fact, $(\mathbf{H}_{\Gamma_d}^e \mathbf{M}_w^{ek})^T$ acts as a means for transferring the nodal forces acting at the external element boundaries to the internal boundary $\Gamma_d{}^e$ (Dias-da-Costa et al. 2009).

The enforcement of the rigid body motion can be made either by using a penalty approach or an Augmented Lagrange Multiplier method. Both methods are taken into account in the work presented in Dias-da-Costa et al. (2009), and lead to the same results. In Dias-da-Costa et al. (2009) it was also found that enforcement of this constraint lacks importance under mesh refinement.

2.3.2 Discretisation in the GFEM

In the *GFEM*, the total displacement field $\mathbf{u}^e$ is the sum of two continuous displacement fields, $\hat{\mathbf{u}}^e$ and $\tilde{\mathbf{u}}^e$. These displacement fields will be associated with two layers of degrees of freedom. The total displacement field is given by:

$$\mathbf{u}^e = \hat{\mathbf{u}}^e + \mathcal{H}_{\Gamma_d} \tilde{\mathbf{u}}^e, \tag{23}$$

and the corresponding finite element approximation is given by:

$$\mathbf{u}^e = \mathbf{N}^e(\mathbf{x}) \left(\hat{\mathbf{a}}^e + \mathcal{H}_{\Gamma_d} \tilde{\mathbf{a}}^e\right) \quad \text{if } \mathbf{x} \in \Omega^e \backslash \Gamma_d, \tag{24a}$$

$$[\![\mathbf{u}]\!]^e = \mathbf{N}^e(\mathbf{x}) \tilde{\mathbf{a}}^e \quad \text{at } \Gamma_d^e. \tag{24b}$$

In Eq. (24b), $\mathbf{N}^e(\mathbf{x})$ are the element shape functions evaluated at Γ_d. Note that this equation is different from Eq. (9b) used in the *DSDA*, in which the jump displacement field is approximated by one-dimensional shape functions defined along the discontinuity.

The nodal displacements are:

$$\mathbf{a}^e = \hat{\mathbf{a}}^e + \mathcal{H}_{\Gamma_d} \tilde{\mathbf{a}}^e, \tag{25}$$

and the strain field is:

$$\boldsymbol{\varepsilon}^e = \mathbf{L}\mathbf{N}^e(\mathbf{x})\mathbf{a}^e = \mathbf{B}^e(\mathbf{x}) \left(\hat{\mathbf{a}}^e + \mathcal{H}_{\Gamma_d} \tilde{\mathbf{a}}^e\right), \tag{26}$$

with the incremental stress field being:

$$d\boldsymbol{\sigma}^e = \mathbf{D}^e \mathbf{B}^e \left(d\hat{\mathbf{a}}^e + \mathcal{H}_{\Gamma_d} d\tilde{\mathbf{a}}^e\right). \tag{27}$$

Incrementally, the tractions are computed by:

$$d\mathbf{t}^e = \mathbf{T}^e d[\![\mathbf{u}]\!]^e = \mathbf{T}^e \mathbf{N}^e d\tilde{\mathbf{a}}^e \text{ at } \Gamma_d^e. \tag{28}$$

Equations (8a) and (8b) can now be discretised:

$$\mathbf{K}_{\hat{a}\hat{a}}^e d\hat{\mathbf{a}}^e + \mathbf{K}_{\hat{a}\tilde{a}}^e d\tilde{\mathbf{a}}^e = d\hat{\mathbf{f}}^e, \tag{29a}$$

$$\mathbf{K}_{\tilde{a}\hat{a}}^e d\hat{\mathbf{a}}^e + \left(\mathbf{K}_{\tilde{a}\tilde{a}}^e + \mathbf{K}_d^e\right) d\tilde{\mathbf{a}}^e = d\tilde{\mathbf{f}}^e, \tag{29b}$$

where

$$\mathbf{K}_{\hat{a}\hat{a}}^e = \int_{\Omega^e \backslash \Gamma_d^e} \mathbf{B}^{eT} \mathbf{D}^e \mathbf{B}^e d\Omega, \tag{30}$$

$$\mathbf{K}_{\hat{a}\tilde{a}}^e = \int_{\Omega^{e+}} \mathbf{B}^{eT} \mathbf{D}^e \mathbf{B}^e d\Omega^e, \tag{31}$$

$$\mathbf{K}_{\tilde{a}\tilde{a}}^e = \mathbf{K}_{\hat{a}\hat{a}}^e = \mathbf{K}_{\hat{a}\tilde{a}}^{eT}, \tag{32}$$

$$\mathbf{K}_d^e = \int_{\Gamma_d^e} \mathbf{N}^{eT} \mathbf{T}^e \mathbf{N}^e d\Gamma, \tag{33}$$

and the force vectors are

$$d\hat{\mathbf{f}}^e = \int_{\Omega^e} \mathbf{N}^{eT} d\bar{\mathbf{b}}^e d\Omega + \int_{\Gamma_t^e} \mathbf{N}^{eT} d\bar{\mathbf{t}}^e d\Gamma, \tag{34a}$$

$$d\tilde{\mathbf{f}}^e = \int_{\Omega^{e+}} \mathbf{N}^{eT} d\bar{\mathbf{b}}^e d\Omega + \int_{\Gamma_t^{e+}} \mathbf{N}^{eT} d\bar{\mathbf{t}}^e d\Gamma. \tag{34b}$$

2.3.3 Discretisation in the discrete-interface approach

In this approach zero thickness interface elements are used. In two dimensions, the interface element is composed by n pairs of nodes as depicted in Fig. 3.

The incremental jump $d[\![\mathbf{u}]\!]^e$ is interpolated according to:

$$d[\![\mathbf{u}]\!]^e = \mathbf{N}_w^e \left[s(\mathbf{x})\right] d\mathbf{w}^e, \tag{35}$$

where $\mathbf{N}_w^e$ contains the interpolation functions, $\mathbf{N}_w^{e^i}$, for each pair of nodes i:

$$\mathbf{N}_w^e = \begin{bmatrix} \mathbf{N}_w^{e^1} & 0 & \cdots & \mathbf{N}_w^{e^n} & 0 \\ 0 & \mathbf{N}_w^{e^1} & \cdots & 0 & \mathbf{N}_w^{e^n} \end{bmatrix}, \tag{36}$$

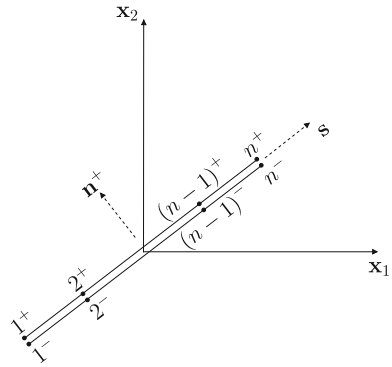

Fig. 3 Interface with n pairs of nodes. Local frame and global frame

The incremental jumps $\mathbf{w}^e$ are computed by taking the difference between top and bottom incremental displacements, for each pair i of nodes:

$$d\mathbf{w}^e = \mathbf{L}_w d\mathbf{a}^e, \tag{37}$$

where $\mathbf{L}_w$ is a $(2n \times 4n)$ matrix, given by:

$$\mathbf{L}_w = \begin{bmatrix} 1 & 0 & -1 & 0 & \cdots & 0 & 0 & 0 & 0 \\ 0 & 1 & 0 & -1 & \cdots & 0 & 0 & 0 & 0 \\ \vdots & \vdots & \vdots & \vdots & \ddots & \vdots & \vdots & \vdots & \vdots \\ 0 & 0 & 0 & 0 & \cdots & 1 & 0 & -1 & 0 \\ 0 & 0 & 0 & 0 & \cdots & 0 & 1 & 0 & -1 \end{bmatrix}, \tag{38}$$

and $d\mathbf{a}^{eT}$ is the vector containing the incremental displacements at the nodes:

$$d\mathbf{a}^{eT} = \left[d\mathbf{a}^e_{1+} \quad d\mathbf{a}^e_{1-} \cdots d\mathbf{a}^e_{n+} \quad d\mathbf{a}^e_{n-} \right]. \tag{39}$$

Replacing Eq. (37) in Eq. (35) the following relation is derived:

$$d[\![\mathbf{u}]\!]^e = \underbrace{\mathbf{N}^e_w \mathbf{L}_w}_{\mathbf{B}^e} d\mathbf{a}^e. \tag{40}$$

The tractions are obtained from the traction-jump law at the discontinuity (see Sect. 3). In incremental format this gives:

$$d\mathbf{t}^{e+} = \mathbf{T}^e d[\![\mathbf{u}]\!]^e = \mathbf{T}^e \mathbf{N}^e_w d\mathbf{w}^e \text{ at } \Gamma^e_d, \tag{41}$$

where $\mathbf{T}^e$ is the discontinuity linearised constitutive relation.

Equation (6) is discretised by means of the field approximations given by Eqs. (40) and (41) leading to:

$$\mathbf{K}^e_{aa} d\mathbf{a}^e = d\mathbf{f}^e, \tag{42}$$

with

$$\mathbf{K}^e_{aa} = \int_{\Gamma_d} \mathbf{B}^{eT} \mathbf{T}^e \mathbf{B}^e d\Gamma, \tag{43}$$

where $\mathbf{K}^e_{aa}$ is the tangential stiffness matrix of the interface element. Prior to opening, integration of the stiffness matrix and the choice of the penalty weights contained in $\mathbf{T}^e$ are of fundamental importance. A high initial penalty stiffness is usually introduced to enforce practically zero jumps and must, simultaneously, guarantee that the traction profile is obtained with the necessary accuracy along and through the discontinuity. Spurious oscillations in the traction profile are avoided adopting Newton-Cotes integration rules with integration points coincident with the nodal positions (Kikuchi and Oden 1988).

3 Material models

The constitutive law for the bulk is linear elastic, whereas the constitutive relations for the discontinuity are detailed in Alfaiate et al. (2002, 2005). For this reason only a brief review is made herein.

3.1 Isotropic damage law

The constitutive relation for the isotropic damage law is given by:

$$\mathbf{t} = (1 - d)\mathbf{T}_{el}[\![\mathbf{u}]\!], \tag{44}$$

where $\mathbf{T}_{el}$ is the elastic matrix, $[\![\mathbf{u}]\!]$ is the jump vector and d is a scalar damage variable, $d \in [0, 1]$, defined by:

$$d = d(\kappa) = 1 - \frac{\kappa_0}{\kappa} \exp\left(-\frac{f_t}{G_F}(\kappa - \kappa_0) \right). \tag{45}$$

In Eq. (45), f_t is the tensile strength, G_F is the fracture energy, k_0 is an initial parameter that denotes the beginning of the softening ($\kappa = \kappa_0$ for $d = 0$) and κ is a scalar variable which is a function of both the normal and the shear jump components, $[\![u]\!]_n$ and $[\![u]\!]_s$, respectively:

$$\kappa = \kappa([\![\mathbf{u}]\!]) = \max \langle [\![u]\!]_n \rangle^+ + \beta \max |[\![u]\!]_s|, \tag{46}$$

where the factor β defines the contribution of the shear jump component to the equivalent jump parameter (Alfaiate et al. 2002).

3.2 Non-isotropic damage law, with shear damage

In this section, a 2-D version of the model introduced in Wells and Sluys (2001b) is reviewed.

The loading function is defined as:

$$f([\![u]\!]_n, \kappa) = [\![u]\!]_n - \kappa, \tag{47}$$

where the internal variable κ is taken as the maximum positive normal relative displacement attained ($\kappa = \max \langle [\![u]\!]_n \rangle^+$), ($\dot{\kappa} \geq 0$).

An exponential softening law is adopted for the constitutive relation between the normal traction component and the normal jump:

$$t_n = \exp\left(-\frac{f_t}{G_F}[\![u]\!]_n\right). \tag{48}$$

The shear traction component t_s is related to the shear jump $[\![u]\!]_s$ according to:

$$t_s = D_{s0} \exp(h_s \kappa)\, [\![u]\!]_s, \tag{49}$$

where D_{s0} is the initial elastic shear stiffness, at crack initiation, and h_s is:

$$h_s = -\ln(D_{s\kappa}/D_{s0}), \tag{50}$$

where $D_{s\kappa}$ is the shear stiffness which is adopted for an advanced state of damage ($\kappa \gg 0$).

3.3 Discontinuity propagation technique in *DSDA* and *GFEM*

It is assumed that the discontinuity is straight and crosses an entire parent element; therefore, the crack tip is always located at the element edge. The direction of the new crack is defined according to the stress state at the tip neighbourhood. In the criterion adopted here, for both the *DSDA* and the *GFEM*, the stress at the tip is evaluated with an averaged tensor, using a Gaussian weight function that smooths out the stresses at the discontinuity tip (Wells and Sluys 2001a):

$$w_i = \frac{1}{(2\pi)^{3/2} l^3} \exp\left(-\frac{r^2}{2l^2}\right). \tag{51}$$

In Eq. (51), w_i is the weight for the respective integration, r is the distance between the integration point and the discontinuity tip, and l is a measure of *significant* distance around the tip. Wells and Sluys (2001a) suggests a value of three times the typical element size, whereas Simone et al. (2003) takes a value equal to four times the length scale of a gradient-enhanced damage model. Here, l is also defined as a length scale parameter: a value of circa 1% of Hillerborg's characteristic length (Hillerborg et al. 1976) is adopted:

$$l_{ch} = \frac{G_F E}{f_t^2}, \tag{52}$$

in which G_F is the fracture energy, f_t is the tensile strength and E is the Young's modulus.

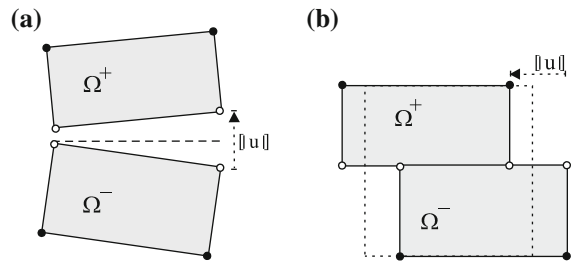

Fig. 4 *DSDA*: **a** mode-I **b** mode-II discontinuity

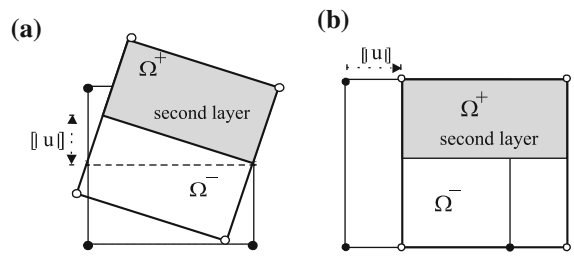

Fig. 5 *GFEM*: **a** mode-I **b** mode-II discontinuity

4 Comparative analysis

4.1 Kinematics and variational formulation

In this Section, the three approaches are compared from the discretisation point of view.

In the *DSDA*, the discontinuity is inserted as if it is an interface element. In Fig. 4 an element crossed by a horizontal discontinuity is represented, in which the black nodes are the regular nodes and the white nodes are the additional nodes. For clarity, a rigid bulk is considered. In Fig. 4a, a split jump is shown and, in Fig. 4b, a shear band is depicted. In the *GFEM*, the number of degrees of freedom of the parent element supporting a discontinuity is doubled, and the enrichment is provided by a second layer of degrees of freedom (see Fig. 5). For comparative purposes, it is possible to define the degrees of freedom in the second layer as the sum of a regular part to a rigid body part. Let:

$$\tilde{\mathbf{a}}^e = \hat{\mathbf{a}}_2^e + \tilde{\mathbf{a}}_{rb}^e, \tag{53}$$

where $\hat{\mathbf{a}}_2^e$ is the regular part and $\tilde{\mathbf{a}}_{rb}^e$ is the rigid body part. The regular deformation is now obtained as:

$$\hat{\mathbf{u}}^e + \hat{\mathbf{u}}_2^e = \mathbf{N}^e(\hat{\mathbf{a}}^e + \mathcal{H}_{\Gamma_d}\hat{\mathbf{a}}_2^e). \tag{54}$$

Thus, in relation to Eq. (9b), it is possible to write:

$$\begin{aligned}\mathbf{u}^e &= \mathbf{N}^e\left[\hat{\mathbf{a}}^e + \mathcal{H}_{\Gamma_d}\tilde{\mathbf{a}}^e\right] \\ &= \mathbf{N}^e\left[\hat{\mathbf{a}}^e + \mathcal{H}_{\Gamma_d}(\hat{\mathbf{a}}_2^e + \tilde{\mathbf{a}}_{rb}^e)\right] \quad \text{in } \Omega\backslash\Gamma_d.\end{aligned} \tag{55}$$

At this stage, three main conclusions can be drawn:

1. the difference between the discretised set of equations derived for *DSDA* and *GFEM* lies in the bulk;
2. the gradient of the additional displacements $\hat{\mathbf{a}}_2^e$ in Ω^+ is non–zero, which is the only reason why separate integration on Ω^+ is necessary;
3. from the kinematics point of view, the *DSDA* may be considered as a particular case of the *GFEM*, in which $\hat{\mathbf{a}}_2^e$ drops, leading to a rigid second layer: $\tilde{\mathbf{a}}^e = \tilde{\mathbf{a}}_{rb}^e$.

In the *DSDA*, the additional nodes are located at the discontinuity, where the quantities of interest are to be measured; therefore, a straight physical interpretation of the additional degrees of freedom is made possible. This formulation is particularly suited for problems in which boundary conditions must be introduced at Γ_d, such as moisture (Alfaiate et al. 2007a,b), temperature or the injection of epoxy resin for crack repairing.

In the *GFEM*, further enrichment is provided from the greater number of degrees of freedom. When compared to the *DSDA*, this leads to an improved capability of evaluating the bulk deformation, but not necessarily to a significantly better description of the kinematics of the discontinuity. In order to emphasize the differences of the discrete-interface approach, the *DSDA* and the *GFEM*, two extreme situations can be defined: *i)* either the discontinuity is much softer than the bulk – the usual situation modelled with a splitting crack and a shear band; or *ii)* the discontinuity is much stiffer than the bulk, as for instance, in the case of a stiff inclusion. In Sect. 5.1, simple examples at element level are presented for these two limit situations.

4.2 Numerical implementation

Each time a discontinuity is inserted, additional degrees of freedom are added both in the *DSDA* and the *GFEM*. Here, in both the *DSDA* and the *GFEM*, only one discontinuity is allowed in each parent finite element; however, both formulations can be extended to include multiple discontinuities (Dias-da-Costa et al. 2009; Daux et al. 2000; Simone et al. 2006).

In order to solve for the equilibrium equations of the body, presented in Sects. 2.3.1 and 2.3.2, it is necessary to compute several numerical integrations, described below. This will be discussed for the external forces, the bulk and the discontinuity, respectively.

Exernal forces As already discussed in Sect. 2.3.1, if the body forces are neglected and all remaining forces are applied at the nodes, $d\mathbf{f}_w^e$ is null in Eq. (22b). Therefore, for the *DSDA*, the evaluation of the integral $\int_{\Gamma_t^{e+}} \mathbf{M}_w^{ekT} \mathbf{N}^{eT} d\bar{\mathbf{t}}^e d\Gamma$ must only be performed when a partially distributed load is applied on Γ_t^{e+}. For the *GFEM* the vector $d\tilde{\mathbf{f}}^e$ in Eq. (34b) must always be evaluated, irrespective of the type of force applied at Γ_t^{e+}.

Bulk For the *DSDA*, the bulk integrals of Eqs. (17) and (18) do not require special consideration since they are extended to the complete domain $\Omega^e \backslash \Gamma_d^e$. For the *GFEM*, the integral in Eqs. (31) and (32) is extended to the subregion Ω^{e+}. For this purpose, the subregion Ω^{e+} is subdivided into triangles, although other approaches have been followed too (Ventura 2006).

Discontinuity The integration of the discontinuity stiffness for the *DSDA* [see Eq. (20)] was already discussed in Dias-da-Costa et al. (2009).

The discontinuity is explicitly inserted into the finite element as if it is an interface element. The stiffness must be numerically integrated in the same way as for the interface elements. The use of the Newton–Cotes/Lobatto scheme is made using two points, which gives the best solutions, in particular if a penalty approach is adopted (Kikuchi and Oden 1988).

In the *GFEM*, the discontinuity is implicitly simulated using the element own shape functions and not the interface element shape functions, according to equations Eqs. (9b) and (24b). This leads to the following: upon mapping into the master element, an initially straight discontinuity may become *curved* (Ventura 2006); being the opposite also true. Note that this *misalignment* of the crack path does not occur in the *DSDA* since a one dimensional interface element is explicitly inserted in the parent element to model the discontinuity. Moreover, special attention must also be paid to the integration scheme adopted, which may give rise to oscillatory solutions if high values of the discontinuity stiffness are used. In order to investigate this issue, a numerical example is presented in Sect. 5.2.5, in which several integration rules are adopted for a high stiffness discontinuity example.

5 Numerical examples

Several examples are computed in order to compare the performance of the three approaches studied. First,

one element examples are presented, in which two different situations are considered: *i*) the discontinuity is significantly softer than the bulk; and *ii*) vice versa. Next, mode-I and mode-II examples are presented, in which the integration of the discontinuity stiffness in the *GFEM* is addressed. In all studied examples plane stress state is assumed. The results obtained with the discrete-interface approach are represented by *DI* while for the remaining formulations the same notation from Sect. 4.2 is adopted.

Hereafter, results in all examples figures are identified in the following manner, concerning the integration scheme: *GFEM*-NC(or G)-n, where 'NC' stands for Newton–Cotes/ Lobatto; 'G' for Gaussian rule; and 'n' is the number of integration points is adopted. For both the discrete-interface approach and the *DSDA*, the Newton–Cotes/Lobatto rule with 2 integration points is adopted, also known as the trapezoidal scheme.

5.1 One element examples

5.1.1 Soft discontinuity with rigid bulk versus rigid discontinuity with soft bulk

A horizontal discontinuity is located at half of the height of the parent element ($1 \times 1 \times 1\,\text{mm}^3$), whereas in the interface model, two finite elements are connected by a zero–thickness interface element. A unit load is applied at the top left node vertically and horizontally, in order to induce mode-I and mode-II crack openings, respectively.

Two situations are simulated: *i*) a soft discontinuity ($k_n = 1\,\text{N/mm}^3$ and $k_s = 10^5\,\text{N/mm}^3$, for mode-I, $k_n = 10^5\,\text{N/mm}^3$ and $k_s = 1\,\text{N/mm}^3$, for mode-II) with a stiffer bulk (Young's modulus, $E = 10^5\,\text{MPa}$; Poisson ratio, $\nu = 0$); and *ii*) a stiffer discontinuity ($k_n = 10^3\,\text{N/mm}^3$ and $k_s = 10^5\,\text{N/mm}^3$, for mode–I, $k_n = 10^5\,\text{N/mm}^3$ and $k_s = 10^3\,\text{N/mm}^3$, for mode–I) with a softer bulk (Young's modulus, $E = 1\,\text{MPa}$; Poisson ratio, $\nu = 0$).

The deformed meshes are shown in Figs. 6, 7a and 7b. The same result is obtained with all formulations in the first case (soft discontinuity), whereas the *DSDA* leads to less bulk deformation in the second case.

If the discontinuity is moved closer to the edge, the corresponding deformed mesh is represented in Fig. 7c. Since the domain Ω^+ becomes smaller, the role of the corresponding subintegrals in Eqs. (29a) and (29b) loses importance, and the *DSDA* and the *GFEM* lead to closer results.

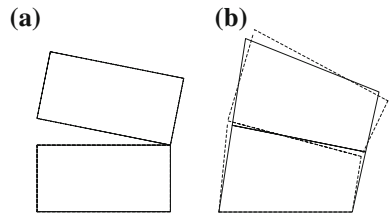

Fig. 6 Mode-I: deformed mesh (reduced 10 times) for the *DSDA* (*continuous*), *DI* and *GFEM* (*dashed*): **a** soft discontinuity; **b** soft bulk

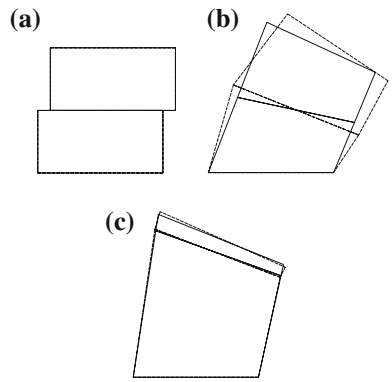

Fig. 7 Mode-II: deformed mesh (reduced 10 times) for the *DSDA* (*continuous*), *DI* and *GFEM* (*dashed*): **a** soft discontinuity; **b** soft bulk; **c** soft discontinuity closer to edge

It can be concluded that for mode-I and mode-II crack opening, in which cases the discontinuities are much softer than the bulk, the results for all formulations are the same. For the soft bulk, both the *GFEM* and the *DI* lead to identical results, whereas less deformation is obtained with the *DSDA*. This is due to the fact that, in the *GFEM* there is an inherent bulk refinement, which can be seen as a sort of remeshing: the superposition of the two layers in the bulk can reproduce the solution obtained with two different elements, as with the interface approach. Additionally, the differences tend to vanish with mesh refinement.

5.1.2 Different integration schemes

Parallel and inclined discontinuities with respect to the element edges are used to study different integration rules. A bilinear finite element is considered with $100 \times 100 \times 100\,\text{mm}^3$. With the *DI* approach, two finite elements (one per side of the discontinuity) are

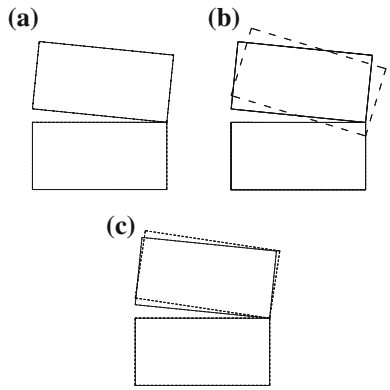

Fig. 8 Deformed mesh ($\alpha = 0°$): **a** *DI*, *DSDA* and *GFEM* for Newton-Cotes/Lobatto with two points (*continuous*); **b** *DI* (*continuous*), *GFEM* for Gauss rule with two points and *GFEM* for Newton-Cotes/Lobatto with three points (*long dashed*); and **c** *DI* (*continuous*) and *GFEM* without inconsistency (*dashed*)

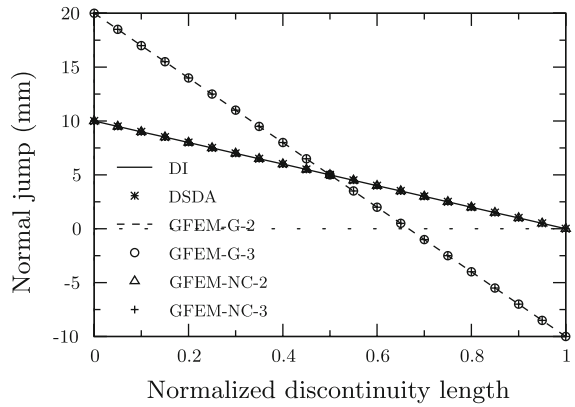

Fig. 9 Normal jump across the discontinuity ($\alpha = 0°$)

connected with a zero-thickness interface element with four nodes. The loading is applied vertically at the top–left node.

Elastic analysis

Both constitutive models adopted for the bulk and for the discontinuity are linear elastic. The Young's modulus is 35 GPa and the Poisson ratio is 0.2. Regarding the discontinuity, a relatively small normal stiffness of 1 N/mm^3 is adopted, together with a shear stiffness of 10^5 N/mm^3.

For a discontinuity parallel to an edge ($\alpha = 0°$), the deformed mesh and jump profiles are represented in Figs. 8 and 9, respectively. A kinematic inconsistency is detected for the *GFEM*, which is related to the integration problems reported by Simone (2004). This kinematic inconsistency vanishes when the Newton-Cotes/Lobatto with two points is used, because the integration points are independent of each other. In order to avoid the negative normal jump at the discontinuity tip, it is also possible: *i*) to keep the nodes that support the tip inactive, or *ii*) to impose additional boundary conditions. The former approach was implemented by Wells and Sluys (2001a); since, in this case, the enhanced degrees of freedom become excessively constrained, the latter approach is followed here. However, in this case an increase in the magnitude of the normal jump is observed. Therefore, the Newton-Cotes/Lobatto with two points integration rule remains the best option for the integration of the discontinuity.

Similar conclusions can be obtained when the discontinuity is inclined with respect to the element edges.

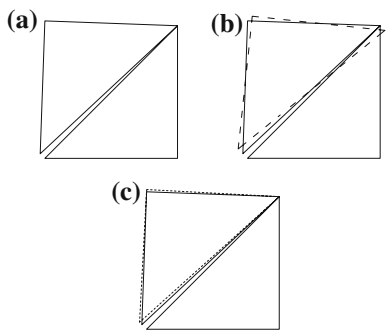

Fig. 10 Deformed mesh ($\alpha = 45°$): **a** *DI*, *DSDA* and *GFEM* for Newton-Cotes/Lobatto with two points (*continuous*); **b** *DI* (*continuous*), *GFEM* for Gauss rule with two points and *GFEM* for Newton-Cotes/Lobatto with three points (*long dashed*); and **c** *DI* (*continuous*) and *GFEM* without inconsistency (*dashed*)

In Fig. 10 the deformed mesh is presented for a discontinuity running under 45°. Newton-Cotes/Lobatto with two points is adequate to perform the numerical integration of the discontinuity stiffness in the *GFEM*. However, when the discontinuity stiffness is made sufficiently high, for instance 10^5 N/mm^3, it becomes evident that 2 integration points are unable to force a null jump along the discontinuity (Fig. 11a). This is a direct consequence of under-integration, which is more pronounced with the Newton-Cotes/Lobatto than with the Gaussian integration rule, both with two points.

For a soft bulk and a rigid discontinuity, for instance adopting a Young's modulus of 35 MPa, the problem mentioned for the Newton-Cotes/Lobatto integration rule with two points becomes even more pronounced. The deformed mesh is represented in Fig. 11b and c.

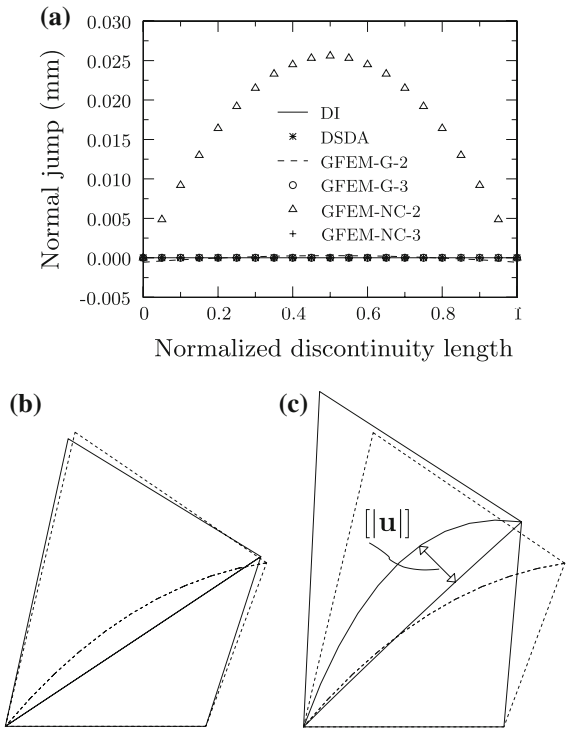

Fig. 11 $\alpha = 45°$: **a** normal jump across the discontinuity; **b** deformed mesh *DSDA* (*continuous*) and *GFEM* Newton-Cotes/Lobatto with two points (*small dashed*); **c** deformed mesh *DSDA* (*continuous*), *GFEM* for Newton-Cotes/Lobatto with three points and *GFEM* for Gauss rule (*small dashed*)

As shown in Fig. 11c an awkward opening of the discontinuity at the center of the element is obtained and it is not possible to impose null jumps at the discontinuity: $\mathbf{N}|_{\Gamma_d}\,\tilde{\mathbf{a}} \neq \mathbf{0}$.

Non-Linear elastic analysis

The example with the discontinuity parallel to the edge is now analysed under mode-I fracture. The material properties are: Young's modulus $E = 35\,\text{GPa}$; Poisson ratio $\nu = 0.2$; tensile strength $f_t = 3.0\,\text{N/mm}^2$; and fracture energy $G_F = 0.1\,\text{N/mm}$. The adopted elastic discontinuity stiffness is $10^5\,\text{N/mm}^3$ for both normal and shear components and an exponential softening law is used.

The vertical displacement of the loaded node is represented in Fig. 12. In all analyses the results obtained with the *DI*, the *DSDA* and the Newton-Cotes/Lobatto with two points are coincident. Furthermore, when the kinematic inconsistency is present, different peak loads are obtained. This is also related to the location of the integration points. When inconsistency is prevented,

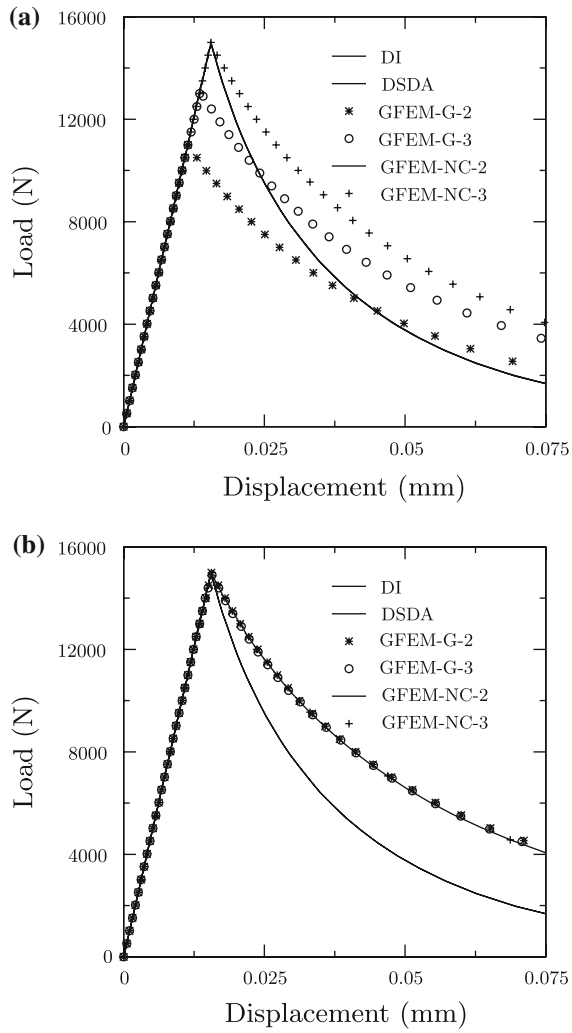

Fig. 12 Vertical displacement of the loaded node: **a** with, and **b** without, kinematic inconsistency

all formulations give rise to the same peak load. Nevertheless, increased displacements are found during softening with the *GFEM*, except for the Newton-Cotes/Lobatto with two points.

The question of which integration rule should be used with *GFEM* becomes less important with a finer mesh. The results are depicted in Fig. 13a for a relatively coarse finite element mesh with 15×15 bilinear elements. A similarity is found, independently of the formulation.

It should be stressed out that, additionally, Newton-Cotes /Lobatto is capable of yielding a continuous traction field across element edges in the *GFEM*. A continuous traction field across element edges always

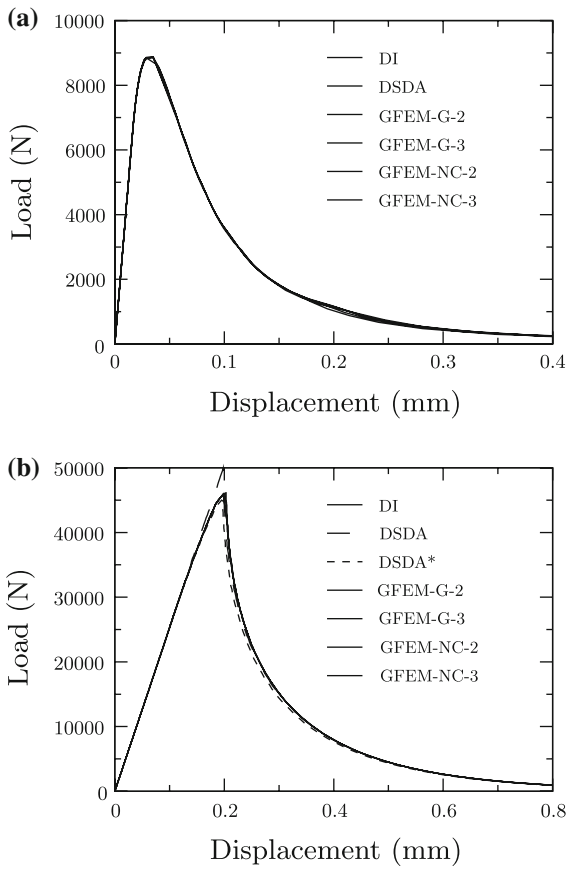

Fig. 13 **a** Load versus vertical displacement for the loaded node; **b** load versus horizontal displacement for the loaded node

occurs with the *DSDA*, independently of the integration rule used for the interface. However, with the *GFEM*, this is only possible if the integration points lie at the element edge.

In the work presented in Dias-da-Costa et al. (2009), it is shown that a rigid body motion jump with the *DSDA* leads to constant shear element jumps. In the following, the mesh from the previous example is used with horizontal loading. The material properties are: cohesion $c_0 = 5.0\,\text{N/mm}^2$; Poisson ratio $\nu = 0.2$; Young's modulus $E = 35\,\text{GPa}$; and fracture energy $G_F = 1.0\,\text{N/mm}$. Exponential softening is adopted.

In Fig. 13b, similar results obtained with all formulations are presented. The exception is the *DSDA*, which presents an increased peak load due to the constraint mentioned above: all integration points are enforced to undergo softening at the same time, as it would happen in a rigid bulk. If the constraint is dropped in the

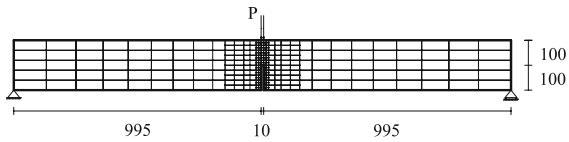

Fig. 14 Three point bending beam (mm)

DSDA, the results become identical to those obtained with other formulations. As already stated in Dias-da-Costa et al. (2009), for a sufficiently refined mesh, it is not necessary to enforce the rigid body motion. In this case, the transmission of the shear jump between the two element crack nodes is automatically performed by the surrounding mesh, except for the last crack node lying at the external boundary.

5.2 Structural examples

5.2.1 Three point bending beam

The first structural example is a three point bending beam, with a span equal to 2 m, where a single notch ($10 \times 100\,\text{mm}^2$) is located at the bottom of the mid–span cross section ($50 \times 200\,\text{mm}^2$), as represented in Fig. 14.

The material properties are: Young's modulus $E = 30\,\text{GPa}$; Poisson ratio $\nu = 0.2$; tensile strength $f_t = 3.33\,\text{MPa}$; fracture energy $G_F = 0.11\,\text{N/mm}$; and both the normal and shear stiffness equal to $10^9\,\text{N/mm}^3$.

The finite element mesh is composed of 270 bilinear finite elements. A total load of 100 kN is applied in the upper part of the beam, according to Fig. 14.

According to the procedure introduced in Sect. 3.3, a new discontinuity is inserted above the notch when the maximum principal stress component at the tip reaches $0.4 f_t$. The direction of crack propagation is evaluated at the tip neighbourhood, using a radius equal to 1% of the characteristic length.

In Fig. 15, the obtained load–vertical displacement curves are shown. The results with three integration points are similar to the ones obtained with two integration points and therefore they are omitted. The possibility of using the *DSDA* with prescribed cracks, replicating a *DI* approach, is exploited. In this case, designated by "prescribed *DSDA*" in Fig. 15a, the discontinuity is inserted a *priori* in the mesh, along the symmetry line. Thus, since the crack path is predefined, the evaluation of the stresses in the bulk at

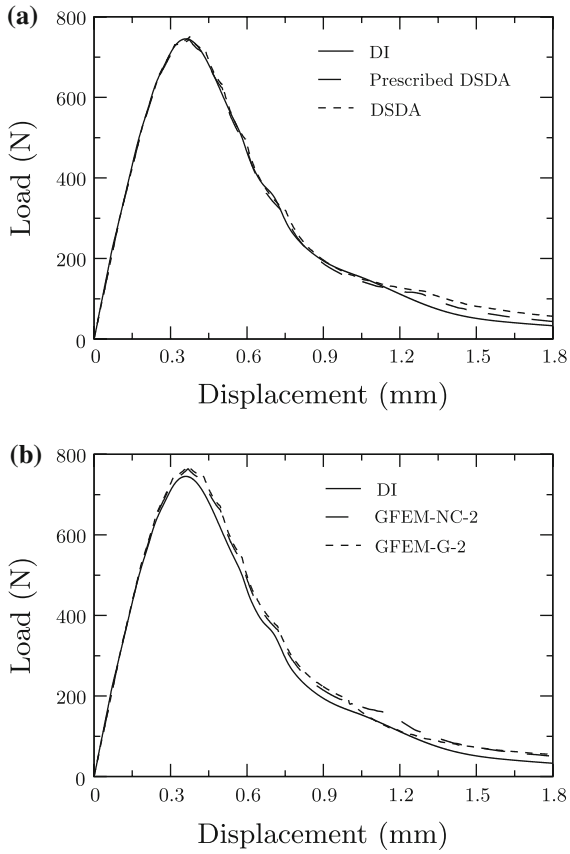

Fig. 15 Three point bending beam: load–vertical displacement curves at the loaded node for **a** *DSDA*, **b** *GFEM*-2

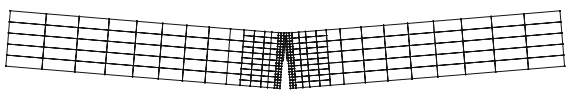

Fig. 16 Three point bending beam: deformed mesh (magnified 100 times), during softening, when the vertical displacement of the loaded node is 0.8 mm

the crack tip is not needed; instead, the tractions are directly evaluated at the discontinuity, based on which the mode-I opening criterion is defined.

The most important conclusion is the similarity between all formulations, in this pure mode-I fracture structural example. Even with a coarse mesh, the load-displacement curves obtained with the *DI* and the *DSDA* are practically coincident, except for the last part of the tail. The *GFEM* results obtained with both two and three integration points are still very close to the *DI* results and all the deformed meshes practically coincide, as shown in Fig. 16.

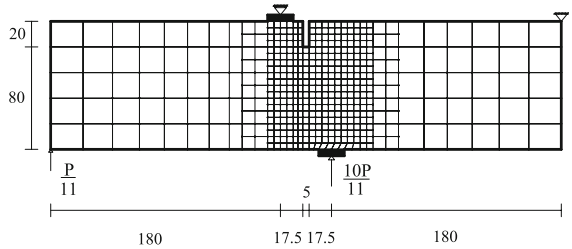

Fig. 17 Single edge notched beam: coarse mesh (mm)

5.2.2 Single edge notched beam

In this Section, a single edge notched beam is simulated (Schlangen 1993). The beam measures $400 \times 100 \times 100\,\text{mm}^3$, and has a $5 \times 20 \times 100\,\text{mm}^3$ notch located at the top, as shown in Fig. 17.

The material parameters are: Young's modulus $E = 35\,\text{GPa}$; Poisson ratio $\nu = 0.15$; tensile strength $f_t = 3.0\,\text{MPa}$; and fracture energy $G_F = 0.1\,\text{N/mm}$. For the discontinuity it is considered a non–isotropic constitutive law (Sect. 3.2) where the normal stiffness is $k_n = 10^5\,\text{N/mm}^3$, whereas the shear stiffness is $k_s = 10^3\,\text{N/mm}^3$.

In Fig. 17, the adopted mesh is represented, consisting of 458 bilinear finite elements. The loading is controlled using the arc length method, in which the monotonic increase of the relative sliding displacement of the notch (CMSD) is enforced.

The direction of crack propagation is evaluated at the tip neighborhood, using a radius equal to $0.5\% l_{ch}$ [Eq. (52)]. A new discontinuity is introduced in each parent element whenever the maximum stress component reaches $0.6 f_t$ at the crack tip.

The obtained crack paths are represented in Fig. 18, whereas the CMSD versus load curves are represented in Fig. 19. The deformed mesh is presented in Fig. 20.

The differences found in the obtained crack paths are near the support. A relatively coarse mesh is adopted and large values of the stress gradients near the support are found. Therefore, a less accurate solution is expected in this particular zone. In Fig. 18, it can be observed that the numerical crack path bends towards the support, whereas the experimental path shifts in the opposite direction. Once again, the results obtained with both the *DSDA* and the *GFEM* are similar.

Finally, only the zone near the support exhibits differences regarding deformations. This is why only the

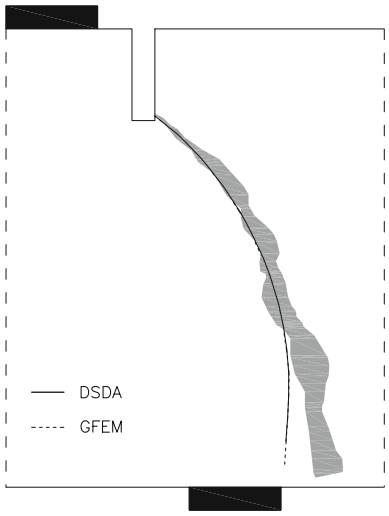

Fig. 18 Single edge notched beam: crack path during softening for $P = 20$ kN, superposed with the experimental envelope (*gray shaded*) for the *DSDA* and *GFEM*

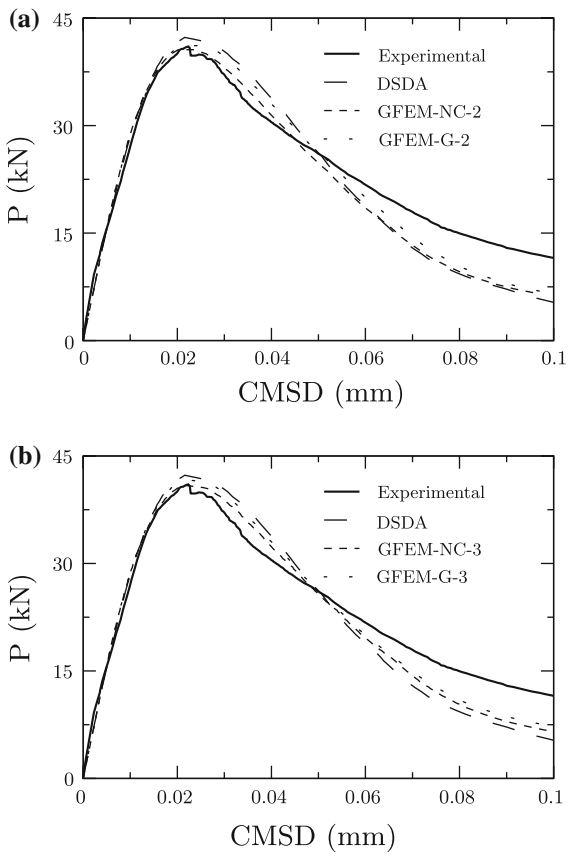

Fig. 19 Single edge notched beam: experimental and *DSDA* load–CMSD curves versus **a** *GFEM*-2 and **b** *GFEM*-3

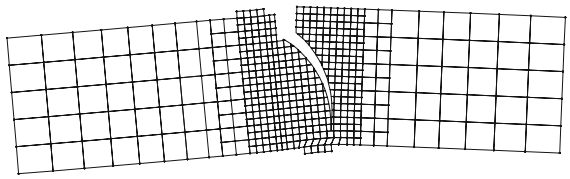

Fig. 20 Single edge notched beam: deformed coarse mesh (magnified 100 times) during softening $P = 20$ kN

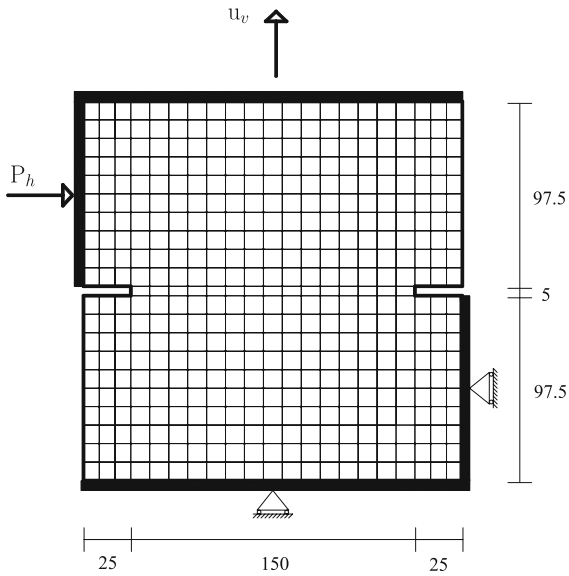

Fig. 21 Mixed mode fracture test: structural scheme, including loading, boundary conditions and mesh (mm)

deformed mesh corresponding to the *DSDA* is shown in Fig. 20.

5.2.3 Nooru-mohamed test

In this section, the numerical analysis of a double-edged-notched specimen submitted to mixed-mode fracture, experimentally tested by Nooru-Mohamed (1992), is presented. The specimen dimensions are $200 \times 200 \times 50$ mm^3, with two $25 \times 5 \times 50$ mm^3 horizontal notches located at half of the height of the specimen as shown in Fig. 21.

The loading is applied at the top of a glued L-shaped steel frame. A horizontal force P_h is then progressively increased until a value of 10 kN is reached. Immediately after, an increasing vertical displacement u_v is imposed, keeping the horizontal force constant (Fig. 21).

The adopted material parameters are taken from Nooru-Mohamed (1992): Poisson ratio $\nu = 0.2$; Young's modulus $E = 30$ GPa; tensile strength $f_t = 3.0$ MPa; and fracture energy $G_F = 0.11$ N/mm. The constitutive law adopted for the discontinuity is the isotropic damage law presented in Sect. 3.1, using a value of $\beta = 0.6$.

The adopted mesh is composed by 435 bilinear finite elements as represented in Fig. 21.

The principal stress direction rotates during the increase of the vertical displacement u_v. Therefore, the discontinuity must be introduced just before crack opening, when the crack orientation is correctly defined. In this test, the discontinuity is propagated when the maximum principal stress component reaches $0.8 f_t$ at the crack tip.

The load–vertical displacement curves are given in Fig. 23. Explanations for the differences could be the consideration of incorrect material parameters as well as spurious bending, leading to different crack paths at the front and rear faces of the specimen (Cervera and Chiumenti 2006; Pivonka et al. 2004; Gasser and Holzapfel 2006). Both the *DSDA* and the *GFEM* formulations are close. The numerically obtained crack paths are practically coincident in all tests performed (see Fig. 22), whereas the load displacement curves coincide until the peak value is reached. The *DSDA* is slightly more brittle in the post-peak behaviour than the *GFEM*.

The deformed meshes are represented in Fig. 24.

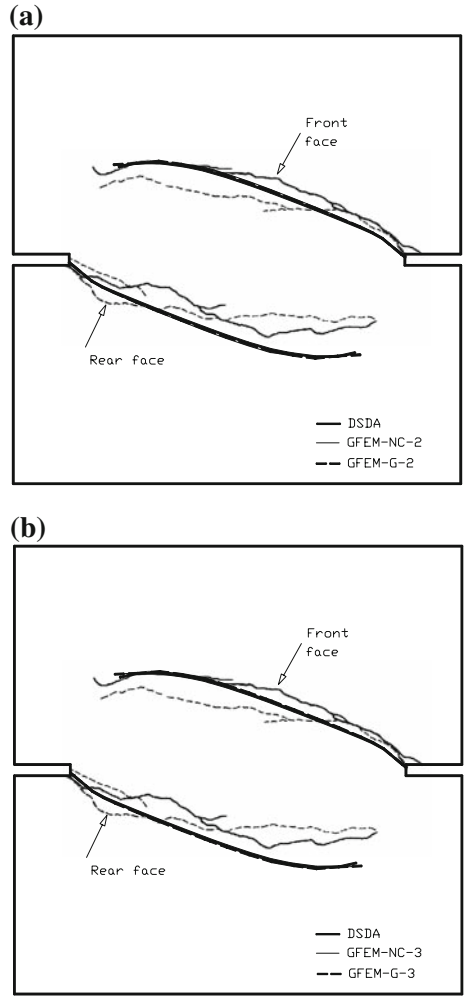

Fig. 22 Crack path, obtained for $u_v = 0.05$ mm, superposed with experimental results taken from Nooru-Mohamed (1992): **a** *DSDA*, *GFEM*-2 and **b** *DSDA*, *GFEM*-3

5.2.4 Prenotched gravity dam model

An experimental test performed by Barpi and Valente (2000) of a dam model is numerically simulated in this Section. The corresponding structural scheme is represented in Fig. 25.

The adopted material parameters are taken from Barpi and Valente (2000): dead-weight $\rho = 2{,}400$ kg/m^3; Young's modulus $E = 35.7$ GPa; Poisson ratio $\nu = 0.1$; tensile strength $f_t = 3.6$ MPa; and fracture energy $G_F = 0.184$ N/mm. Additionally, the discontinuity is assumed to open in mode-I, with the shear stiffness suddenly dropping to zero when softening is reached.

The mesh is composed of 1848 bilinear finite elements (see Fig. 25). A refinement is performed near the notch in order to better evaluate the stress at the discontinuity.

The dead load is first applied; afterwards the water pressure in front of the dam is gradually increased. During the loading, the arc length method is used to enforce an increase of the relative crack mouth opening displacement (CMOD). The crack is inserted when the averaged stress tensor at the tip reaches $0.7 f_t$, for a radius of 1% of the characteristic length l_{ch} [Eq. (52)].

The results are represented in Figs. 26 and 27. The results obtained with the *DSDA* and *GFEM* formulations are similar. Additionally, there is a good agreement with the experimental crack paths and the numerical results represented with the thickest lines. Moreover, when the load versus CMOD curves are compared, the elastic stage and peak loads are obtained

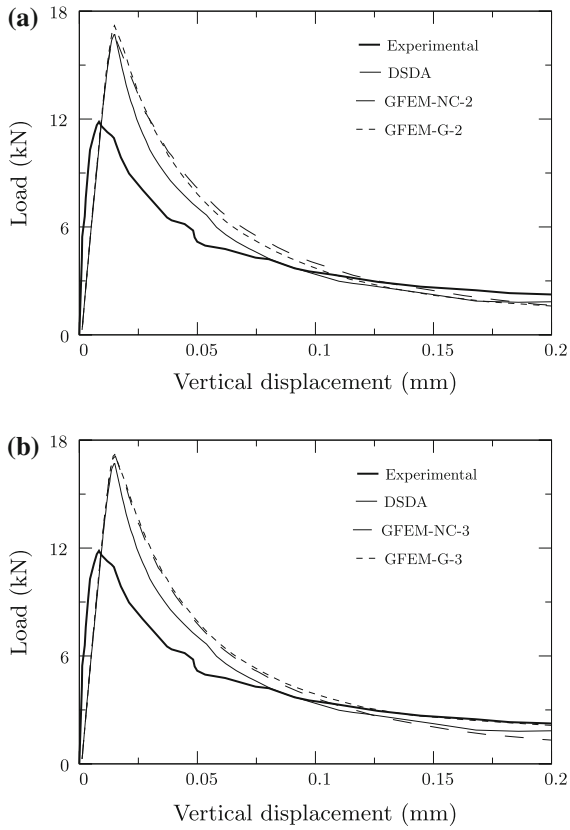

Fig. 23 Mixed mode fracture test: Load versus vertical displacement superposed with experimental results (Nooru-Mohamed 1992) for the *DSDA* and: **a** *GFEM*-2 and **b** *GFEM*-3

with accuracy. However, during softening, it is found that the model is not able to capture the mixed mode behaviour and, therefore, numerically the load decays faster than experimentally. It must also be emphasized that during softening the numerical results approach Barpi and Valente's curve (Barpi and Valente 2000).

The deformed mesh for the *DSDA* is represented in Fig. 28, when the CMOD is 0.25 mm.

5.2.5 Simulation of crack repair test

Simone (2004) presented some results concerning different integration schemes for the *GFEM*, following Rots (1988) example for interface elements. The same example was already tackled by Dias-da-Costa et al. (2009) for the *DSDA*. Here this example is again addressed to compare the *DSDA* to the *GFEM*; however, a different interpretation is proposed. Suppose that the beam was first loaded and a central traction-free

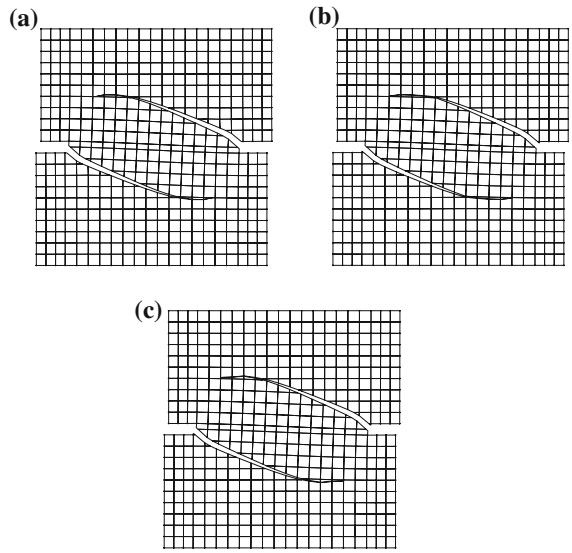

Fig. 24 Deformed mesh (magnified 100 times), when $u_v = 0.05$ mm: **a** *DSDA*, **b** *GFEM* for Newton-Cotes/Lobatto with two points and **c** *GFEM* for Newton-Cotes/Lobatto with three points and *GFEM* for Gauss rule

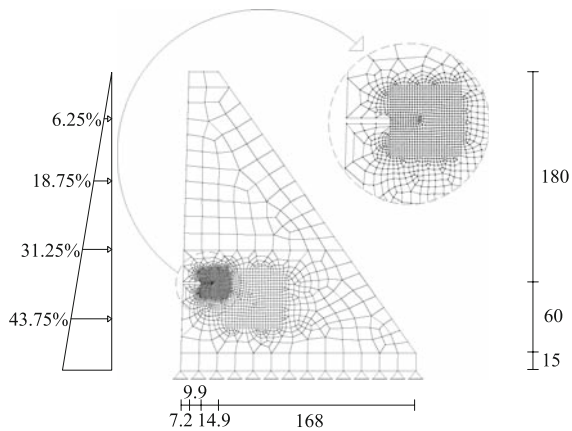

Fig. 25 Prenotched gravity dam model: structural scheme, including loading, boundary conditions and mesh (cm)

crack developed. After alleviating the load, this crack was repaired with epoxy and the beam was reloaded. In the beginning of the test, before other cracks develop, the results would correspond to the ones presented below.

In Fig. 29, the structural scheme for the notched beam studied is presented, with the following bulk material properties: Young's modulus $E = 20$ GPa and Poisson ratio $\nu = 0.2$. The discontinuity constitutive relation is linear elastic. In order to simulate the stiffness introduced by the epoxy, different penalty param-

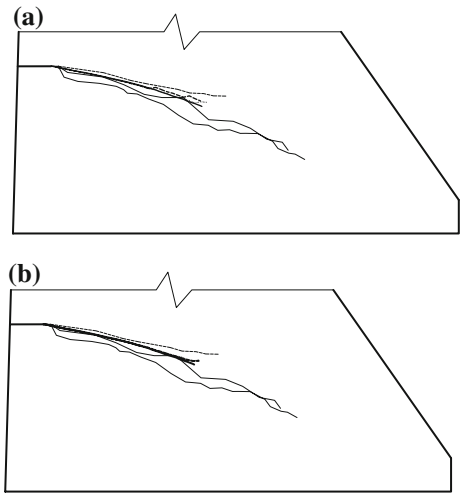

Fig. 26 Crack path, obtained when CMOD is 0.25 mm, superposed with experimental and numerical results taken from Barpi and Valente (2000): **a** *DSDA* (*thick line*), Newton-Cotes/Lobatto with two points (*thick dashed line*), *GFEM* for two points (*doted line*); and **b** *DSDA* (*thick line*), Newton-Cotes/Lobatto with three points (*thick dashed line*), *GFEM* for three points (*doted line*)

eters are adopted for the elastic stiffness, $k_n = k_s$: 10^3,10^4,10^5 and 10^8 MPa/mm. The notch is simulated with null stiffness.

The beam is subjected to a load of 1 kN. A structured and an unstructured mesh (see Fig. 29) are studied. In both cases, bilinear finite elements are used and the notch depth is equal to 20 mm.

From Fig. 30 it can be concluded that, similarly to the discrete-interface approach, the use of the Newton–Cotes/ Lobatto with the *DSDA* effectively avoids traction oscillations. For the penalization range tested, the results are almost independent of the applied penalty value. In this figure, the differences found in the smoothness of the traction profiles are due to the different mesh size.

The results obtained with the *GFEM* are represented in Figs. 31 and 32. Note that the results for the Gauss rule are omitted because the conclusions are similar to the Newton-Cotes/Lobatto rule with 3 integration points. It is found that Newton-Cotes/Lobatto using two points is the integration scheme that gives the greatest stability to results, both for regular and irregular meshes. In all other cases, it is not possible to use a penalty parameter of 10^8 MPa/mm. Therefore, the *GFEM* should not be applied with high penalty values for the discontinuity stiffness. Moreover, as already stated by Simone (2004), the Newton-Cotes/Lobatto

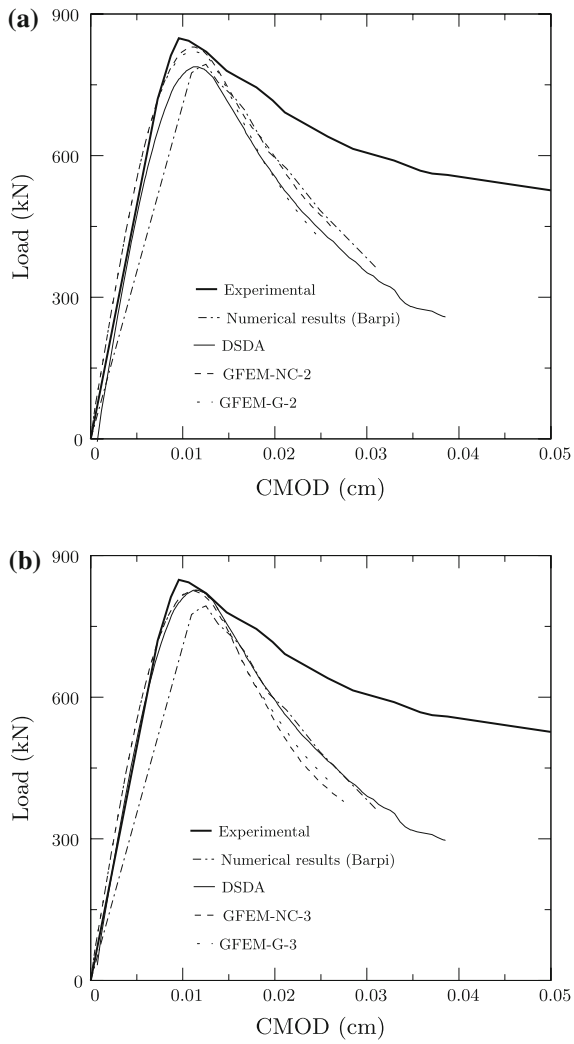

Fig. 27 Prenotched gravity dam model: Load versus CMOD superposed with experimental results (Barpi and Valente 2000) for the *DSDA* and: **a** *GFEM*-2 and **b** *GFEM*-3

can significantly reduce the level of oscillations which are obtained with the Gaussian rule in the *GFEM*.

6 Conclusions

In this paper, three different formulations used to model strong discontinuities are compared: the *DSDA*, the *GFEM* and the discrete-interface approach. It is shown that all three approaches present advantages and disadvantages, such that their usefulness depend on the problem at hand.

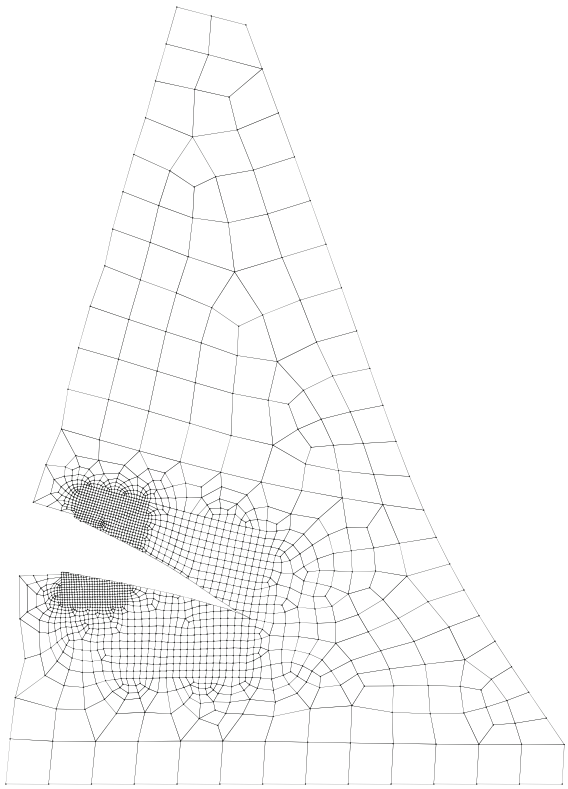

Fig. 28 Prenotched gravity dam model: deformed mesh (magnified 1,000 times), during softening, when the CMOD is 0.35 mm

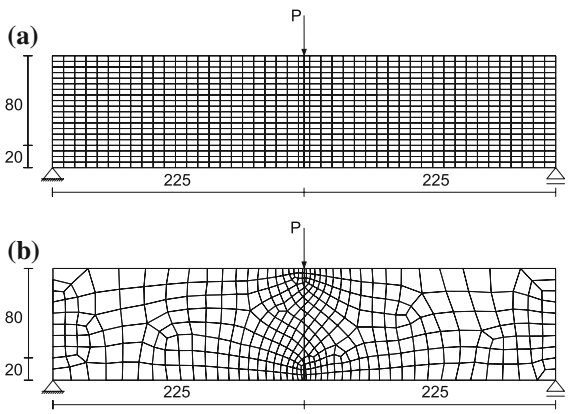

Fig. 29 Structural scheme of the notched beam with 100 mm width (all dimension in mm) and mesh used for the numerical tests: **a** structured mesh and **b** unstructured mesh

The discrete-interface approach is preferred for the modelling of fixed geometric discontinuities, such as bond-slip interfaces between concrete and internal or external reinforcement, old concrete-new concrete interfaces, mixed structures, masonry joints, etc.. However, the use of this approach gives rise to numerical difficulties in non-prescribed crack problems, namely remeshing.

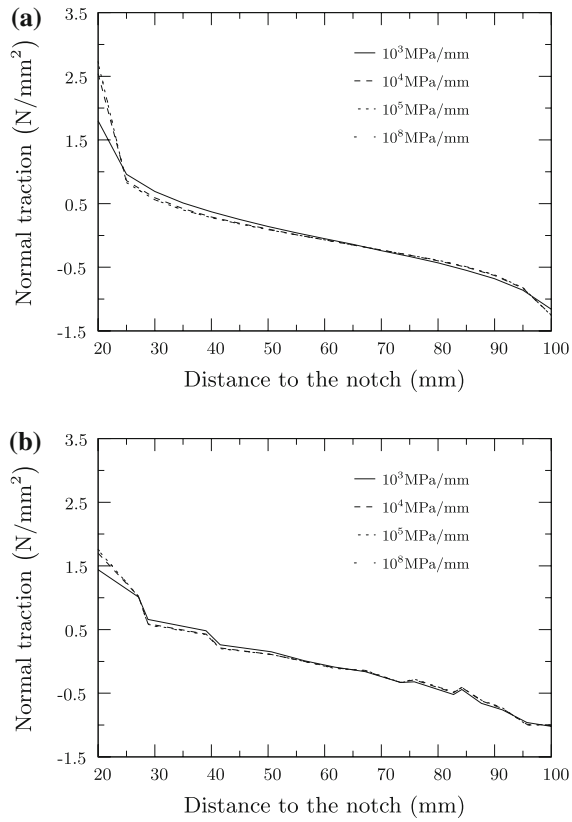

Fig. 30 Traction profile in front of the notch of the beam with the *DSDA* for: **a** structured mesh and **b** unstructured mesh for different penalty parameters

Conversely, both the *DSDA* and the *GFEM* overcome this problem since the discontinuity is located in the parent finite element, independently of mesh orientation. Towards a unified view of the *DSDA* and the *GFEM*, some shared properties can be put forward, namely:

- both can be built upon the same variational formulation;
- in both cases, the additional degrees of freedom are global;
- the kinematics of the *DSDA* can be interpreted as a particular case of the kinematics of the *GFEM* in which a second rigid layer is adopted;
- in quasi–brittle materials, when the discontinuity is considerably softer than the bulk, both the *DSDA*

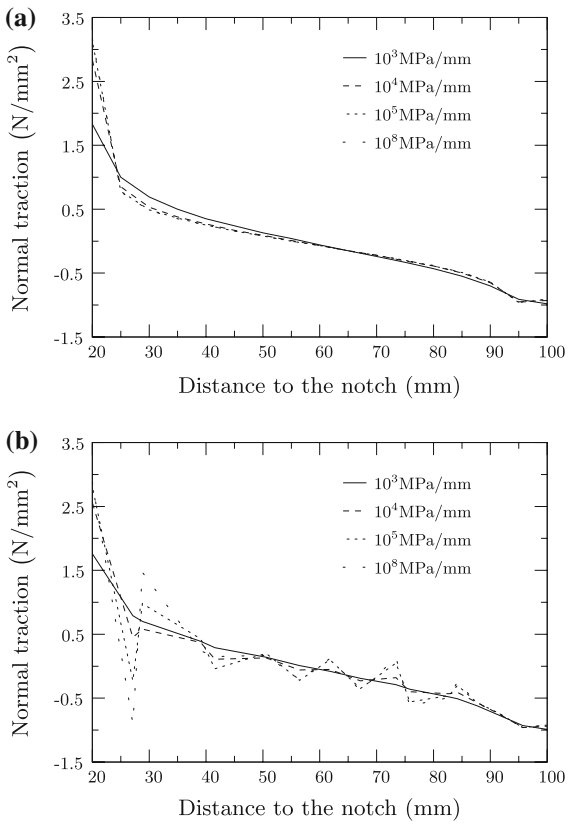

Fig. 31 Traction profile in front of the notch of the beam with *GFEM* and Newton-Cotes/Lobatto with two points for: **a** structured mesh and **b** unstructured mesh

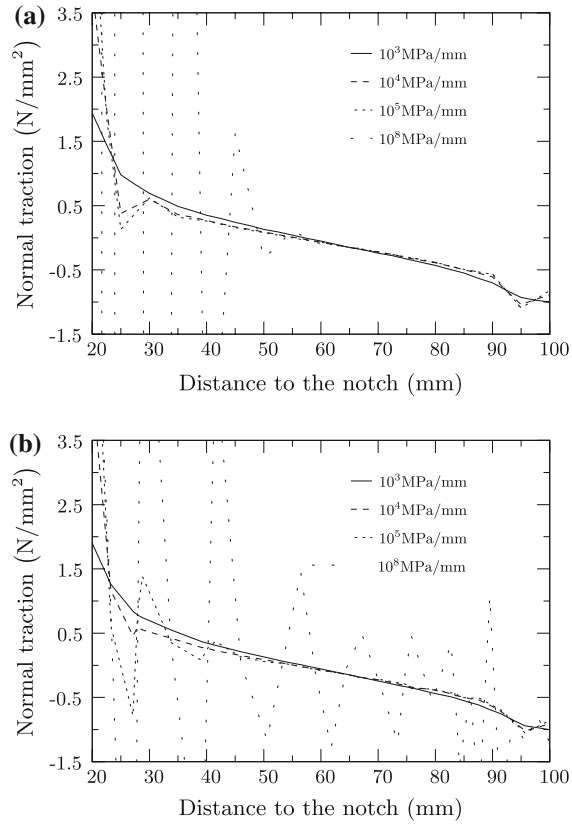

Fig. 32 Traction profile in front of the notch of the beam with *GFEM* and Newton-Cotes/Lobatto with three points for: **a** structured mesh and **b** unstructured mesh

and the *GFEM* give rise to similar results, even if coarse meshes are used.

However, some important differences were also found, such as:

- in the *DSDA*, the discontinuity is explicitly modelled as an interface element, using the same one-dimensional shape functions. As a result, integration along the discontinuity does not pose any numerical problems; this is why these formulations should be preferred with stiff discontinuities, namely penalty formulations or cracks repaired with injection of epoxy resin;
- the additional nodes in the *DSDA* are located at the discontinuity, where the quantities of interest are to be measured, giving rise to a straight physical interpretation of the additional degrees of freedom;
- as a consequence, continuity of the traction field is automatically obtained across element boundaries and problems in which boundary conditions must be explicitly introduced at the discontinuity, such as moisture, temperature or crack repairing with epoxy, benefit from such implementation;
- the *DSDA* is simple to implement; in particular, no integration on Ω^+ is necessary.

With respect to the *GFEM*:

- sub-integration on Ω^+ is necessary, which can be interpreted as a sort of remeshing, although certainly more favourable than the usual one since no additional elements are defined;
- the discontinuity is implicitly described by means of the shape functions of the finite element. As a consequence, integration along the discontinuity can lead to numerical problems, namely stress oscillations and awkward opening modes. In particular, it is found that the *GFEM* is not adequate to be used with stiff discontinuities, due to the lack of numerical robustness;

– the *GFEM* is based on the partition of unity concept: additional degrees of freedom are introduced at the nodes to reproduce the kinematics of complex continua; as a consequence, the *GFEM* provides an inherent better refinement of the bulk.

Acknowledgments The authors acknowledge the financial support of the Portuguese Science and Technology Foundation (FCT), PhD Grant number SFRH/BD/40349/2007.

References

Alfaiate J, Sluys L (2005) Discontinuous numerical modelling of fracture using embedded discontinuities. In: Owen DRJ, Nate EO, Suárez B (eds) Computational plasticity, fundamentals and applications. COMPLAS VIII, Barcelona, Spain

Alfaiate J, Sluys LJ (2004) On the use of embedded discontinuities in the framework of a discrete crack approach. In: Yao Z, Yuan WZM (eds) Sixth international congress on computational mechanics in conjunction with the second asian-pacific congress of computational mechanics. WCCMVI, Beijing, China

Alfaiate J, Pires EB, Martins JAC (1992) A finite element model for the study of crack propagation. In: Aliabadi MH, Cartwright DJ, Nisitani H (eds) 2nd international conference on localised damage, Computational Mechanics Publications and Elsevier Applied Science. Southampton, United Kingdom, pp 261–282

Alfaiate J, Pires EB, Martins JAC (1997) A finite element analysis of non-prescribed crack propagation in concrete. Comput Struct 63(1):17–26

Alfaiate J, Wells GN, Sluys LJ (2002) On the use of embedded discontinuity elements with crack path continuity for mode-I and mixed-mode fracture. Eng Fract Mech 69(6):661–686

Alfaiate J, Simone A, Sluys LJ (2003) Non-homogeneous displacement jumps in strong embedded discontinuities. Int J Solids Struct 40(21):5799–5817

Alfaiate J, Sluys LJ, Pires EB (2005) Mixed mode fracture in concrete and masonry. In: Ferro AC, Mai Y, Ritchie RG (eds) ICFXI, 11th international conference on fracture, Torino, Italy

Alfaiate J, Moonen P, Sluys LJ (2007a) On the use of DSDA and X-FEM for the modelling of discontinuities in porous media. In: Oñate E, Owen DRJ (eds) IX International Conference on Computational Plasticity.. COMPLAS IX, Barcelona, Spain

Alfaiate J, Moonen P, Sluys LJ, Carmeliet J (2007b) On the modelling of preferential moisture uptake in porous media. In: EPMESC XI, Kyoto, Japan

Areias P, Belytschko T (2005) Analysis of three-dimensional crack initiation and propagation using the extended finite element method. Int J Numer Methods Eng 63:760–788

Armero F, Garikipati K (1996) An analysis of strong discontinuities in multiplicative finite strain plasticity and their relation with the numerical simulation of strain localization in solids. Int J Solids Struct 33(20–22):2863–2885

Barenblatt G (1962) The mathematical theory of equilibrium cracks in brittle fracture. Adv Appl Mech 7:55–129

Barpi F, Valente S (2000) Numerical simulation of prenotched gravity dam models. J Eng Mech 126(6):611–619

Bazant ZP, Oh BH (1983) Crack band theory of concrete. Mater Struct 16:155–177

Belytschko T, Black T (1999) Elastic crack growth in finite elements with minimal remeshing. Int J Numer Methods Eng 45(5):601–620

Bocca P, Carpinteri A, Valente S (1986) Mixed mode fracture of concrete. Int J Solids Struct 27:1139–1153

Bolzon G (2001) Formulation of a triangular finite element with an embedded interface via isoparametric mapping. Comput Mech 27(6):463–473

Borja RI (2008) Assumed enhanced strain and the extended finite element methods: a unification of concepts. Comput Methods Appl Mech Eng 197(33–40):2789–2803

Carey GF, Ma M (1999) Joint elements, stress post-processing and superconvergent extraction with application to Mohr–Coulomb failure. Commun Numer Methods Eng 15(5):335–347

Carol I, Prat P (1995) A multicrack model based on the theory of multisurface plasticity and two fracture energies. In: Owen DRJ, Oñate E, Hinton E (eds) Computational Plasticity, fundamentals and applications. Pineridge Press, Barcelona, Spain , pp 1583–1594

Cervera M, Chiumenti M (2006) Smeared crack approach: back to the original track. Int J Numer Anal Methods Geomech 30(12):1173–1199

Dias-da-Costa D, Alfaiate J, Sluys LJ, Júlio E (2009) A discrete strong discontinuity approach. Eng Fract Mech 76(9):1176–1201

Daux C, Moës N, Dolbow J, Sukumar N, Belytschko T (2000) Arbitrary branched and intersecting cracks with the extended finite element method. Int J Numer Methods Eng 48(12):1741–1760

Duarte CAM, Oden JT (1995) H-p clouds-an h-p meshless method. Tech Rep 95–05

Duarte CAM, Babuška I, Oden JT (2000) Generalized finite element methods for three-dimensional structural mechanics problems. Comput Struct 77(2):215–232

Dugdale DS (1960) Yielding of steel sheets containing slits. J Mech Phys Solids 8(2):100–104

Dvorkin EN, Cuitiño AM, Gioia G (1990) Finite elements with displacement interpolated embedded localization lines insensitive to mesh size and distortions. Int J Numer Methods Eng 30(3):541–564

Gasser TC, Holzapfel GA (2006) 3d crack propagation in unreinforced concrete: a two-step algorithm for tracking 3d crack paths. Comput Methods Appl Mech Eng 195(37–40):5198–5219

Goodman RE, Taylor RL, Brekke TL (1968) A model for the mechanics of jointed rock. J Soil Mech Found Div 99:637–659

Herrmann LR (1978) Finite element analysis of contact problems. ASCE J Eng Mech Div 104(5):1043–1057

Hillerborg A, Modeer M, Petersson PE (1976) Analysis of crack formation and crack growth in concrete by means of fracture mechanics and finite elements. Cem Concr Res 6(6):773–781

Ingraffea A (1989) Shear cracks. In: Elfgren L (ed) Fracture mechanics of concrete structures—from theory to applications, report of the Technical Committee 90-FMA Fracture Mechanics of Concrete-Applications. Chapman and Hall, London, United Kingdom , pp 231–233

Ingraffea A, Saouma V (1985) Numerical modelling of discrete crack propagation in reinforced and plain concrete. In: Sih GC, DiTommaso A (eds) Engineering Application of Fracture Mechanics. Martinus Nijhoff Publishers,

Jirásek M, Belytschko T (2002) Computational resolution of strong discontinuities. In: Mang HA, Rammerstorfer JEFG (ed) WCCM V, Fifth world congress on computational mechanics, Vienna, Austria

Kikuchi N, Oden JT (1988) Contact problems in elasticity: a study of variational inequalities and finite element methods. SIAM Studies in Applied Mathematics 8, Philadelphia

Klisinski M, Runesson K, Sture S (1991) Finite element with inner softening band. J Eng Mech 117(3):575–587

Larsson R, Runesson K (1996) Element-embedded localization band based on regularized displacement discontinuity. J Eng Mech 122(5):402–411

Linder C, Armero F (2007) Finite elements with embedded strong discontinuities for the modeling of failure in solids. Int J Numer Methods Eng 72(12):1391–1433

Lofti HR, Shing PB (1995) Embedded representation of fracture in concrete with mixed finite elements. Int J Numer Methods Eng 38(8):1307–1325

Lourenço P, Rots JG (1997) A multi-surface interface model for the analysis of masonry structures. ASCE J Eng Mech 123(7):660–668

Malvern LE (1969) Introduction to the mechanics of a continuous medium. Prentice-Hall International, Englewood Cliffs, New Jersey

Melenk JM, Babuška I (1996) The partition of unity finite element method: basic theory and applications. Comput Methods Appl Mech Eng 139(1–4):289–314

Moës N, Dolbow J, Belytschko T (1999) A finite element method for crack growth without remeshing. Int J Numer Methods Eng 46(1):131–150

Moës N, Sukumar N, Moran B, Belytschko T (2000) An extended finite element method (x-fem) for two- and three-dimensional crack modeling. In: ECCOMAS 2000, Barcelona

Nooru-Mohamed MB (1992) Mixed-mode fracture of concrete: an experimental approach. PhD thesis, Delft University of Technology

Ohlsson U, Olofsson T (1997) Mixed-mode fracture and anchor bolts in concrete analysis with inner softening bands. J Eng Mech 123(10):1027–1033

Oliver J (1996) Modelling strong discontinuities in solid mechanics via strain softening constitutive equations. part 1: fundamentals. Int J Numer Methods Eng 39(21):3575–3600

Oliver J, Huespe AE, Pulido MDG, Chaves E (2002) From continuum mechanics to fracture mechanics: the strong discontinuity approach. Eng Fract Mech 69:113–136

Oliver J, Huespe AE, Sanchez PJ (2006) A comparative study on finite elements for capturing strong discontinuities: E-FEM vs X-FEM. Comput Methods Appl Mech Eng 195(37–40):4732–4752

Pivonka P, Ozbolt J, Lackner R, Mang HA (2004) Comparative studies of 3d-constitutive models for concrete: application to mixed-mode fracture. Int J Numer Methods Eng 60(2):549–570

Remmers JJC (2006) Discontinuities in materials and structures: a unifying computational approach. PhD thesis, Delft University of Technology

Rots JG (1988) Computational modeling of concrete fracture. PhD thesis, Delft University of Technology

Sancho J, Planas J, Gálvez J, Cendón D, Fathy A (2005) Three-dimensional simulation of concrete fracture using embedded crack elements without enforcing crack path continuity. In: Owen DRJ, nate EO, Suárez B (eds) Computational plasticity, fundamentals and applications. COMPLAS VIII, Barcelona, Spain

Schlangen E (1993) Experimental and numerical analysis of fracture processes in concrete. PhD thesis, Delft University of Technology

Simo JC, Rifai MS (1990) A class of mixed assumed strain methods and the method of incompatible modes. Int J Numer Methods Eng 29(8):1595–1638

Simo JC, Oliver J, Armero F (1993) An analysis of strong discontinuities induced by strain-softening in rate-independent inelastic solids. Comput Mech 12:277–296

Simone A (2004) Partition of unity-based discontinuous elements for interface phenomena: computational issues. Commun Numer Methods Eng 20(6):465–478

Simone A, Wells GN, Sluys LJ (2003) From continuous to discontinuous failure in a gradient-enhanced continuum damage model. Comput Methods Appl Mech Eng 192(41–42):4581–4607

Simone A, Duarte CAM, Van der Giessen E (2006) A generalized finite element method for polycrystals with discontinuous grain boundaries. Int J Numer Methods Eng 67(8):1122–1145

Tijssens MGA, Sluys LJ, Van der Giessen E (2000) Numerical simulation of quasi-brittle fracture using damaging cohesive surfaces. Eur J Mech, A/Solids 19(5):761–779

Ventura G (2006) On the elimination of quadrature subcells for discontinuous functions in the extended finite-element method. Int J Numer Methods Eng 66(5):761–795

Wells GN, Sluys LJ (2000) Application of embedded discontinuities for softening solids. Eng Fract Mech 65(2–3):263–281

Wells GN, Sluys LJ (2001a) A new method for modelling cohesive cracks using finite elements. Int J Numer Methods Eng 50(12):2667–2682

Wells GN, Sluys LJ (2001b) Three-dimensional embedded discontinuity model for brittle fracture. Int J Solids Struct 38(5):897–913